

Very long period seismic signatures of unsteady eruptions predicted from conduit flow models

Katherine R. Coppess¹, Eric M. Dunham^{2,3}, Martin Almquist⁴

¹Department of Physics, Stanford University, CA, USA

²Department of Geophysics, Stanford University, CA, USA

³Institute of Computational and Mathematical Engineering, Stanford University, Stanford, CA, USA

⁴Department of Information Technology, Division of Scientific Computing, Uppsala University, Sweden

Key Points:

- We provide expressions for the seismic force in eruptions that can be evaluated using outputs from unsteady conduit flow models.
- We generate and analyze seismograms from vulcanian eruption models to identify the seismic expression of fragmentation and other processes.
- Our modeling suggests that eruptive mass could be inferred by extending seismic inversions to periods of minutes to tens of minutes.

Corresponding author: Katherine R. Coppess, kcoppess@stanford.edu

Abstract

Explosive volcanic eruptions radiate seismic waves as a consequence of pressure and shear traction changes within the conduit/chamber system. Kinematic source inversions utilize these waves to determine equivalent seismic force and moment tensor sources, but relation to eruptive processes is often ambiguous and nonunique. In this work, we provide an alternative, forward modeling approach to calculate moment tensor and force equivalents of a model of eruptive conduit flow and chamber depressurization. We explain the equivalence of two seismic force descriptions, the first in terms of traction changes on the conduit/chamber walls, and the second in terms of changes in magma momentum, weight, and momentum transfer to the atmosphere. Eruption onset is marked by a downward seismic force, associated with loss of restraining shear tractions from fragmentation. This is followed by a much larger upward seismic force from upward drag of ascending magma and reduction of magma weight remaining in the conduit/chamber system. The static force is upward, arising from weight reduction. We calculate synthetic seismograms to examine the expression of eruptive processes at different receiver distances. Filtering these synthetics to the frequency band typically resolved by broadband seismometers produces waveforms similar to very long period (VLP) seismic events observed in strombolian and vulcanian eruptions. However, filtering heavily distorts waveforms, accentuating processes in early, unsteady parts of eruptions and eliminating information about longer time scale depressurization and weight changes that dominate unfiltered seismograms. The workflow we have introduced can be utilized to directly and quantitatively connect eruption models with seismic observations.

Plain Language Summary

Volcanic eruptions radiate seismic waves that can be recorded by seismometers placed on and around a volcano. Analysis of seismic data enables one to study eruptions, in particular the processes occurring in the magma-filled conduit and chamber that feeds the eruption. One process of particular interest is fragmentation, in which magma containing a mixture of liquid melt and gas bubbles breaks apart in the conduit and erupts explosively from the vent. We perform computer simulations of explosive eruptions and then use the output of those simulations to predict seismic radiation. We examine the seismograms produced by this workflow to identify features that are diagnostic of process, such as fragmentation, that occur at different times in the eruption. These predictions will guide interpretation of seismic data from real eruptions.

1 Introduction

Seismic monitoring of active volcanoes is a widely used geophysical technique to remotely detect and study eruptions. Seismic radiation from volcanic eruptions occurs across a wide frequency band, with higher frequency radiation arising from turbulence and particle-wall interactions within the conduit (Fee, Haney, et al., 2017), volcano-tectonic (VT) fracture events (Roman & Cashman, 2006), and other impulsive or short-duration processes. Eruptions often also feature very long period (VLP) seismic signals that are simpler, usually involving just one or a few cycles of oscillatory motion on broadband seismometers when high-pass filtered above ~ 0.01 Hz as is common in most studies. VLP radiation is generally attributed to coherent processes associated with magma movement, pressure and shear traction changes, and inflation or deflation of dikes, sills, and other magma storage structures in the volcanic plumbing system (McNutt & Roman, 2015; Kawakatsu & Yamamoto, 2015; B. A. Chouet & Matoza, 2013). Unraveling VLP seismic waveforms, and relating them to these eruptive processes, thereby provides insight into the fluid dynamics and internal structure of volcanoes.

Typical analysis of VLP seismograms is done using kinematic waveform inversion to determine an effective moment tensor and single force time history from which the

eruptive source process is inferred (McNutt & Roman, 2015; Kawakatsu & Yamamoto, 2015; B. A. Chouet & Matoza, 2013). Kinematic inversions have been performed on many volcanoes. Studies of vulcanian eruptions often reveal inflation/deflation sources at depths of ~ 1 -2 km, as seen in Popocatepetl, Mexico (B. Chouet et al., 2005), Augustine, Alaska (Dawson et al., 2011), and Redoubt, Alaska (Haney et al., 2013), for example. Shallow sources have also been observed, such as at Asama, Japan (Maeda et al., 2019), which are commonly interpreted as inflation/deflation of cracks within the hydrothermal system. VLP sources in strombolian eruptions also span a range of depths, from ~ 1 km at Yasur (Matoza et al., 2022) to just a few hundred meters at Stromboli. The source at Stromboli may involve both moment and forces (Ripepe et al., 2021) or just moment contributions from pre-eruptive pressurization and expansion of the cylindrical conduit followed by depressurization and contraction during eruption (Legrand & Pertont, 2022). In many of these studies, there is often ambiguity regarding the presence of a force component in addition to a moment source. The 2004 eruption of Asama provides some of the most convincing evidence for a vertical force from vulcanian eruptions (Ohminato et al., 2006). VLP studies have also been conducted for caldera collapse events, such as the recent 2018 eruption of Kilauea (Lai et al., 2021), and interpreted in terms of frictional slip on a ring fault bounding the unsteadily dropping caldera block and pressurization of an underlying magma chamber (Wang et al., 2021). Kinematic inversions have also provided insights into other volcanic events involving ring faulting and intrusions (Fukao et al., 2018; Fontaine et al., 2019; Sandanbata et al., 2021).

However, the interpretation of moment tensor and force sources can be nonunique and only ambiguously related to eruptive processes (Dawson et al., 2011). In addition, there appears to be some confusion in the literature regarding the origin of the single force component, which has been variably attributed to changes in magma momentum (i.e., inertia) or tractions on the walls of the conduit and chamber system. Single force models have been utilized to describe seismic sources involving transient decoupling of a solid or fluid region from the rest of the Earth. Examples include landslides (Kanamori & Given, 1982; Eissler & Kanamori, 1987; Hasegawa & Kanamori, 1987; Dahlen, 1993; Allstadt, 2013), spalling from shallow explosions (Day & McLaughlin, 1991), iceberg calving events (Tsai et al., 2008; Nettles & Ekström, 2010; Murray et al., 2015), pyroclastic flows (Uhira & Takeo, 1994; Yamasato, 1997; De Angelis et al., 2007), and volcanic eruptions (Kanamori et al., 1984; Takeo et al., 1990; Uhira & Takeo, 1994; Ripepe et al., 2021). While the seismic representation theorem has been generalized in a manner that explains the origin of equivalent force and moment sources from fluid motions and other processes (Takei & Kumazawa, 1994, 1995), it has been challenging to connect that representation to commonly used volcanic source descriptions such as conduit flow models. An important advance toward this was provided by Brodsky et al. (1999), building on Kanamori and Given (1982), who derived an expression for the seismic force in terms of changes in the magma momentum, weight, and momentum transfer to the atmosphere in the context of the 1980 eruption of Mount St. Helens. This was done using a global momentum balance applied to a control volume encompassing the conduit and chamber, which while correct limits the applicability to point source descriptions of an eruption.

Here we provide a theoretical derivation and workflow to calculate equivalent seismic moment and force histories from unsteady conduit flow and depressurizing chamber models, which can then be used to generate synthetic seismograms. The derivation is based on an extension of the work of Burridge et al. (1993) on seismic radiation from pressure changes in a fluid-filled borehole to account also for changes in shear traction when that fluid is viscous. We also account for radiation from a magma chamber connected to the base of the conduit. An important insight provided by our work is the equivalence of expressions for the single force in terms of either tractions on the walls of the conduit and chamber (the traction-based representation) or changes in magma momentum, weight, and momentum transfer to the atmosphere (the inertial representation).

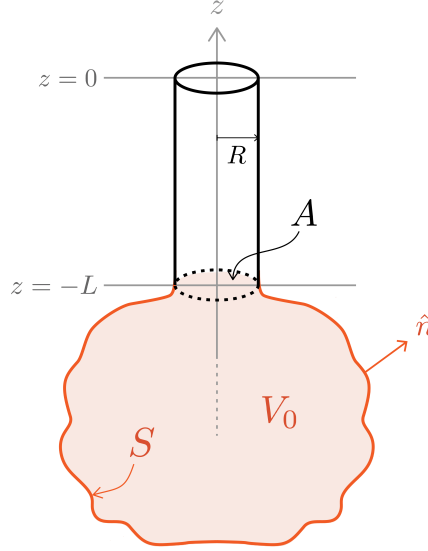


Figure 1. Schematic representation of conduit-chamber system: a vertical, cylindrical conduit of radius R and length L connected to chamber with initial volume V_0 . We define the surface enclosing V_0 as the union of the conduit-chamber opening A and the magma-solid Earth interface S with surface normal vector \hat{n} .

Following the derivation, we apply the workflow to compute seismic radiation from vulcanian-type explosions idealized with a quasi-1D model of unsteady, two-phase conduit flow coupled to a lumped parameter magma chamber. We examine the relative contributions of force and moment sources from the conduit and chamber, exploring how processes like fragmentation are expressed in the seismic waveforms. This overall workflow opens the possibility of performing seismic source inversions directly for the eruptive processes using conduit flow models, circumventing the need to first perform a kinematic source inversion.

2 Summary of workflow

We begin by summarizing a key outcome of our study: a workflow to generate synthetic seismograms from an unsteady quasi-1D conduit flow model. Steady state conduit flow models have time-independent tractions on the solid and hence do not produce seismic radiation. We assume a vertical cylindrical conduit of radius R and cross-sectional area $A = \pi R^2$, venting to the atmosphere and connected to a magma chamber of nominal volume V_0 at the base of the conduit (Figure 1). The conduit is centered on the z axis, with $z = 0$ being the vent, $z = -L$ being the top of the chamber, and z positive upward. Elastic compliance of the walls is negligible in comparison to magma compressibility for this geometry (Costa et al., 2007), so we assume rigid walls in the conduit flow model. We model the magma chamber using a lumped parameter model that assumes spatially uniform pressure changes within the chamber, derived from the chamber mass balance with outflow from the chamber to conduit. Relevant details of the conduit and chamber models are provided in the next section.

- I. Solve the conduit flow and chamber depressurization model. This provides the changes in pressure $\Delta p(z, t)$ and shear traction (i.e., wall shear stress) $\Delta \tau(z, t)$ in the conduit, as well as the change in chamber pressure $\Delta p_{ch}(t)$.

- II. Use the source representation (see Appendix A) to convert the conduit pressure change into a moment tensor per unit depth,

$$\frac{dM_{ij}(z, t)}{dz} = \frac{A\Delta p(z, t)}{\mu} [(\lambda + 2\mu)\delta_{ij} - 2\mu\delta_{iz}\delta_{jz}], \quad (1)$$

where λ is the first Lamé parameter and μ is shear modulus; and the shear traction change into a force per unit depth,

$$\frac{dF_i(z, t)}{dz} = \delta_{iz}2\pi R\Delta\tau(z, t). \quad (2)$$

Treating the chamber as a spherical point source, convert the chamber pressure change into a moment tensor source (Aki & Richards, 2002; Ichihara et al., 2016),

$$M_{ij}^{ch}(t) = \frac{3V_0\Delta p_{ch}(t)}{4} \left(\frac{\lambda + 2\mu}{\mu} \right) \delta_{ij}. \quad (3)$$

This expression can be replaced with moment tensors for nonspherical chambers (e.g., Segall, 2010). There is also a force contribution from momentum exchange between conduit and chamber and the change in chamber magma weight $\Delta M_{ch}(t)g$:

$$F_i^{ch}(t) = [-A\Delta p_{ch}(t) - \Delta M_{ch}(t)g] \delta_{iz}. \quad (4)$$

- III. Convolve the moment and force distributions with the Green's function $G_{ij}(\mathbf{x}, \mathbf{x}', t)$ of the elastic wave equation to produce synthetic seismograms:

$$\begin{aligned} u_i(\mathbf{x}, t) = & \int_{-L}^0 \left[\frac{dM_{jk}(z', t)}{dz'} * \frac{\partial G_{ij}(\mathbf{x}, \mathbf{x}', t)}{\partial x'_k} + \frac{dF_j(z', t)}{dz'} * G_{ij}(\mathbf{x}, \mathbf{x}', t) \right] dz' \\ & + M_{jk}^{ch}(t) * \frac{\partial G_{ij}(\mathbf{x}, \mathbf{x}', t)}{\partial x'_k} \Big|_{\mathbf{x}'=\mathbf{x}_{ch}} + F_j^{ch}(t) * G_{ij}(\mathbf{x}, \mathbf{x}_{ch}, t), \end{aligned} \quad (5)$$

where $*$ denotes time convolution, the Green's functions in the conduit integrand are evaluated on the z' axis, and \mathbf{x}_{ch} is the chamber centroid. This treats the chamber as a point source. When seismic wavelengths are sufficiently long (Aki & Richards, 2002), then the point source approximation can be used for the conduit contribution, too, in which case (5) becomes

$$\begin{aligned} u_i(\mathbf{x}, t) = & M_{jk}^{co}(t) * \frac{\partial G_{ij}(\mathbf{x}, \mathbf{x}', t)}{\partial x'_k} \Big|_{\mathbf{x}'=\mathbf{x}_{co}} + F_j^{co}(t) * G_{ij}(\mathbf{x}, \mathbf{x}_{co}, t) \\ & + M_{jk}^{ch}(t) * \frac{\partial G_{ij}(\mathbf{x}, \mathbf{x}', t)}{\partial x'_k} \Big|_{\mathbf{x}'=\mathbf{x}_{ch}} + F_j^{ch}(t) * G_{ij}(\mathbf{x}, \mathbf{x}_{ch}, t), \end{aligned} \quad (6)$$

where $M_{ij}^{co}(t)$ and $F_i^{co}(t)$ are obtained by integrating the conduit moment and force per unit depth over the length of the conduit. Strictly speaking, spatially variable force will provide a vertical vector dipole contribution to the conduit moment tensor. However, we anticipate this will be small in comparison to other contributions to the moment tensor, so we neglect it in this work.

The above workflow is specific to cylindrical conduits of constant cross-sectional area; an additional contribution to the vertical force will arise when the cross-sectional area varies with depth. Another important generalization is to account for the finiteness of the chamber, rather than treating it as a point source.

The remainder of our study is devoted to justifying the source representation, deriving expressions relating the seismic force to eruptive processes in the conduit and chamber, and then applying the workflow for several conduit flow example problems.

3 Equivalent expressions for seismic force and connection to global momentum balance

Volcano seismology studies have variably attributed the seismic force component of the source representation to shear tractions on the conduit walls and to changes in the momentum of magma within the conduit. Here we explain the relation between these two conceptual interpretations. We also show that when the local momentum balance is integrated over the conduit and chamber, we obtain the global momentum balance identified by Brodsky et al. (1999) in their study of the 1980 Mount St. Helens eruption. In addition we account for time variations of the magma momentum, which were neglected by Brodsky et al. (1999). Furthermore, we isolate contributions from the conduit and magma chamber, whereas Brodsky et al. (1999) combined them together into a single control volume.

3.1 Conduit momentum balance

While our workflow is applicable to any quasi-1D conduit flow model that provides pressure and shear traction changes on the conduit walls, we specialize the discussion and derivation to follow to models in which all phases and components are co-moving with a common pressure and particle velocity. The momentum balance is

$$\rho \left(\frac{\partial v}{\partial t} + v \frac{\partial v}{\partial z} \right) = - \frac{\partial p}{\partial z} - \rho g - \frac{2\tau}{R}, \quad (7)$$

where ρ is density, v is vertical particle velocity, p is pressure, τ is wall shear stress, and g is the gravitational acceleration. At this point we place no restrictions on the specific form of the equation of state and model for wall shear stress. The momentum balance is paired with the source-free continuity equation,

$$\frac{\partial \rho}{\partial t} + \frac{\partial(\rho v)}{\partial z} = 0. \quad (8)$$

Next we add Av times (8) to A times (7) to obtain the momentum balance in conservation form:

$$A \frac{\partial(\rho v)}{\partial t} + A \frac{\partial(p + \rho v^2)}{\partial z} = -A\rho g - 2\pi R\tau. \quad (9)$$

Seismic radiation and static displacements arise from changes in pressure and shear traction about some initial state. For this initial state, we assume the magma is at rest with the initial pressure gradient balancing the weight of the magma and shear traction from a plug:

$$A \frac{\partial p_0}{\partial z} = -A\rho_0 g - 2\pi R\tau_0. \quad (10)$$

The subscript 0 indicates values from the initial state. We subtract (10) from (9) to obtain the perturbation momentum balance:

$$A \frac{\partial(\rho v)}{\partial t} + A \frac{\partial(\Delta p + \rho v^2)}{\partial z} = -A\Delta\rho g - 2\pi R\Delta\tau, \quad (11)$$

where $\Delta = \text{present state} - \text{initial state}$. Finally, we integrate (11) along the length of the conduit to obtain the global momentum balance for the conduit:

$$\begin{aligned} \frac{d}{dt} \left[A \int_{-L}^0 \rho v dz \right] &= A(\Delta p + \rho v^2)|_{z=-L} - A(\Delta p + \rho v^2)|_{z=0} \\ &\quad - \int_{-L}^0 A\Delta\rho g dz - \int_{-L}^0 2\pi R\Delta\tau dz. \end{aligned} \quad (12)$$

This can be rewritten using a more compact notation:

$$\dot{P}_{co} = F_{ch \rightarrow co} - F_{vent} - \Delta M_{co}g - F_{co}, \quad (13)$$

where P_{co} is the momentum of the conduit magma, the rate of momentum transfer from the chamber to the conduit is

$$F_{ch \rightarrow co} = A(\Delta p + \rho v^2)|_{z=-L}, \quad (14)$$

and the rate of momentum imparted to the atmosphere at the conduit vent is

$$F_{vent} = A(\Delta p + \rho v^2)|_{z=0}. \quad (15)$$

The third contribution to the change in conduit momentum arises from mass erupting out of the vent leading to a reduction in weight; the change in weight is $\Delta M_{co}g$, where

$$\Delta M_{co} = \int_{-L}^0 A \Delta \rho dz = -A \int_0^t (\rho v)|_{z=-L}^{z=0} dt, \quad (16)$$

with the latter expression following from the conduit mass balance. And finally, there is momentum exchange with the surrounding solid through the change in restraining forces (shear tractions) at the conduit walls. This includes frictional drag between the flowing magma and conduit walls and the loss of shear traction during rupture of a plug. Using Newton's third law pairs, we define the change in force exerted by the magma on the solid Earth along the conduit walls as

$$F_{co} = \int_{-L}^0 2\pi R \Delta \tau dz, \quad (17)$$

which will be one contribution to the seismic force.

3.2 Chamber momentum balance

We treat the chamber vertical momentum balance in a similar manner, quantifying changes relative to an initial magmastatic reference state. In this derivation of the seismic force contribution from the chamber, it is essential to go beyond commonly used lumped parameter chamber models with spatially uniform pressure. We therefore consider nonlinear flow of compressible magma within a chamber of arbitrary shape, but, as for the conduit, restrict attention to models in which all phases and components have a common stress tensor and particle velocity. Let $V(t)$ be the chamber volume in the current state. We assume that changes to the chamber volume are small compared to the initial volume, which allows us to linearize geometry changes around the initial (reference) state. The chamber volume in the reference state is V_0 ; its surface is split into two parts (Figure 1). The first part, denoted by S and having unit outward normal \hat{n} , is the interface between the chamber magma and the surrounding solid. The second part is the surface connecting the chamber and the conduit at $z = -L$, denoted as A and having unit outward normal in the $+z$ direction. We assume that chamber magma starts from rest, with magma weight determining the initial pressure gradient:

$$\frac{\partial p_0}{\partial z} = -\rho_0 g. \quad (18)$$

The vertical momentum balance during the eruption is

$$\rho \left(\frac{\partial v_z}{\partial t} + v_i \frac{\partial v_z}{\partial x_i} \right) = \frac{\partial \sigma_{iz}}{\partial x_i} - \rho g \quad (19)$$

where v_i is the particle velocity and the stress tensor σ_{ij} includes both an isotropic pressure and deviatoric stresses associated with flow of the viscous magma. Then, we add to (19) v_z times the continuity equation with no internal mass sources,

$$\frac{\partial \rho}{\partial t} + \frac{\partial(\rho v_i)}{\partial x_i} = 0, \quad (20)$$

to obtain the momentum balance in conservation form:

$$\frac{\partial(\rho v_z)}{\partial t} + \frac{\partial(\rho v_z v_i)}{\partial x_i} = \frac{\partial \sigma_{iz}}{\partial x_i} - \rho g. \quad (21)$$

Next, subtract (18) from (21) and denote changes with respect to the reference state using the same Δ notation as for the conduit, e.g., $\Delta \sigma_{ij} = \sigma_{ij} + p_0 \delta_{ij}$. Then integrate over V , using V_0 when appropriate for our linearized deformation model, and apply the divergence theorem to obtain the global momentum balance of the chamber magma:

$$\begin{aligned} \frac{d}{dt} \int_{V_0} \rho v_z d^3x &= \int_{(S+A)} (\Delta \sigma_{iz} - \rho v_z v_i) n_i d^2x - \int_V \Delta \rho g d^3x \\ &= \int_S \Delta \sigma_{iz} n_i d^2x - A(\Delta p + \rho v^2)|_{z=-L} - \int_V \Delta \rho g d^3x. \end{aligned} \quad (22)$$

In going to the second expression, we have neglected advective momentum transfer through the chamber walls ($\rho v_z v_i n_i = 0$ on S) and utilized the interface conditions with the conduit on the surface A , namely,

$$\int_A \rho v_z d^2x = \rho v A|_{z=-L} \quad (23)$$

and

$$\int_A (\Delta \sigma_{zz} - \rho v_z^2) d^2x = -A(\Delta p + \rho v^2)|_{z=-L}, \quad (24)$$

where ρ , v , and Δp appearing on the right side of the equations above are for the conduit magma. We denote the global momentum balance as

$$\dot{P}_{ch} = -F_{ch} - F_{ch \rightarrow co} - \Delta M_{ch} g. \quad (25)$$

In this expression, P_{ch} is the total vertical momentum of magma within the chamber. The vertical component of the force exerted by the chamber magma on the surrounding solid is

$$F_{ch} = - \int_S \Delta \sigma_{iz} n_i d^2x, \quad (26)$$

which will be the second contribution to the seismic force. This includes contributions from spatially nonuniform pressure as well as shear tractions along the chamber walls. The rate of momentum transfer from the chamber to conduit, $F_{co \rightarrow ch}$, is identical to the definition given earlier in the context of the conduit momentum balance, namely equation (14). The change in chamber magma weight is $\Delta M_{ch} g$, where

$$\Delta M_{ch} = \int_V \Delta \rho d^3x = - \int_0^t \int_A \rho v_z d^2x dt = -A \int_0^t (\rho v)|_{z=-L} dt, \quad (27)$$

with the second expression following from the chamber mass balance and the third, involving ρ and v at the base of the conduit, resulting from the interface condition (23).

3.3 Global momentum balance and expressions for seismic force

We then add the global momentum balances for the conduit (12) and chamber (25) to obtain the global magma momentum balance for the conduit and chamber system:

$$\dot{P} = -F_{vent} - \Delta M g - F_s, \quad (28)$$

where we have defined the rate of change of the magma momentum as $\dot{P} = \dot{P}_{co} + \dot{P}_{ch}$, the total change in magma weight as $\Delta M g = \Delta M_{co} g + \Delta M_{ch} g$, and the seismic force $F_s = F_{co} + F_{ch}$. Note that magma momentum and magma weight refer only to contributions from magma that remains within the subsurface conduit-chamber system, excluding magma that has been erupted; the erupted mass is $-\Delta M$. We return to this point shortly when discussing the momentum balance of the atmosphere.

Seismic radiation within the solid Earth can only be generated through contact forces (i.e., ones acting along the interface between the magma and the surrounding solid), which we use to define the traction-based representation for the seismic force F_s :

$$F_s = F_{co} + F_{ch}. \quad (29)$$

An alternative expression for F_s can be obtained by using the total magma momentum balance (28):

$$F_s = -\dot{P} - F_{vent} - \Delta Mg. \quad (30)$$

We refer to this as the inertial-based representation. Seismic forces are not solely caused by changes in magma momentum; they are also dependent on the conduit-atmosphere momentum exchange and the change in weight of the magma in the conduit and chamber. Equation (30) matches the expression for seismic force derived by Brodsky et al. (1999). They then neglected magma momentum changes \dot{P} and weight changes $-\Delta Mg$ and approximated F_{vent} as $-\rho v^2 A$. This yields $F_s \approx -\rho v^2 A$, evaluated at the vent, which can also be written as $F_s = -\dot{M}v$ where $\dot{M} = \rho v A$ is the eruptive mass rate. This expression was the basis of a workflow using seismic estimates of F_s to infer \dot{M} and then plume height (Prejean & Brodsky, 2011). This approximation neglects the $\Delta p A$ term in F_{vent} , as well as changes in magma momentum and weight. Our example simulations to follow suggest that this approximation is not well justified, at least for the parameter space we have explored.

3.4 Momentum conservation of the conduit-chamber-atmosphere-solid Earth system

The momentum balance concepts applied to the conduit and chamber magma can be equally well applied to the atmosphere and solid Earth. Their global vertical momentum balances are

$$\dot{P}_{atm} = F_{vent} + \Delta Mg - F_{surf} \quad (31)$$

and

$$\dot{P}_{solid} = F_s + F_{surf}, \quad (32)$$

where the total vertical momentum of the atmosphere and solid Earth are P_{atm} and P_{solid} , $-\Delta Mg$ is the change in weight of the atmosphere (which is opposite in sign to the subsurface magma weight change due to mass conservation), and F_{surf} is the change in force exerted by the atmosphere on the solid Earth surface. Momentum conservation of the entire system is obtained by summing (28), (31), and (32) to show that

$$\dot{P} + \dot{P}_{atm} + \dot{P}_{solid} = 0, \quad (33)$$

as expected.

In many eruptions, the eruptive fluid rises within a buoyant plume and is then distributed horizontally over time scales that are much longer than are relevant for the seismic radiation problem. The addition of mass to the atmosphere and its increase of weight must be compensated for by a slight increase in atmospheric pressure, which acting on the solid Earth surface provides the force change F_{surf} . The long time scale of this process, as well as the large horizontal length scales over which F_{surf} acts, justifies neglecting F_{surf} in comparison to F_s when calculating seismic radiation from eruptions. Exceptions to this may arise if the eruption column collapses into a pyroclastic flow and/or lahars, and in this case one must connect with the growing body of work studying seismic wave generation by these sources (e.g., Uhira & Takeo, 1994; Yamasato, 1997; De Angelis et al., 2007; Kumagai et al., 2009; Allstadt, 2013; Zobin et al., 2009; Lai et al., 2018).

3.5 Specialization to lumped parameter chamber model

Many volcano modeling studies, including the example models in this work, utilize lumped-parameter models of magma chambers within which changes to the stress

tensor take the form of a spatially uniform change in chamber pressure, p_{ch} (e.g., Segall, 2010). The chamber mass balance, combined with the magma equation of state and an elastic deformation model for the solid bounding the chamber, leads to an evolution equation for the change in chamber pressure. The linearized version of this model is

$$\beta V_0 \frac{dp_{ch}}{dt} = -Q, \quad (34)$$

where β is the combined chamber and magma compressibility and Q is the volumetric flow rate of magma from the chamber into the conduit. When coupling this model to the conduit model given by equations (7) and (8), we use the conditions

$$Q(t) = Av(-L, t) \quad \text{and} \quad p_{ch}(t) = p(-L, t). \quad (35)$$

The latter condition neglects viscous or turbulent pressure loss as magma enters the conduit as well as the nonlinear advective momentum transport term ρv^2 that appeared in the more general coupling condition (24).

This chamber model neglects contributions to the chamber momentum balance from magma momentum changes (i.e., $\dot{P}_{ch} = 0$), such that (25) reduces to

$$0 = -F_{ch} - F_{ch \rightarrow co} - \Delta M_{ch} g. \quad (36)$$

Thus in the examples to follow, we calculate the chamber contribution to the seismic force as

$$F_{ch} = -F_{ch \rightarrow co} - \Delta M_{ch} g, \quad (37)$$

with

$$F_{ch \rightarrow co} = A \Delta p|_{z=-L} = A \Delta p_{ch} \quad (38)$$

and

$$\Delta M_{ch} = -A \int_0^t \rho v|_{z=-L} dt. \quad (39)$$

4 Example simulation

In this section, we apply the workflow stated in section 2 to a representative simulation from an unsteady conduit flow model. We discuss the force and moment histories and then present synthetic seismograms at various distances using Green's functions for a homogeneous elastic half-space. We note that far more sophisticated conduit flow models exist, which account for processes thought to be relevant to certain eruption styles or magmas, but we choose to use a simple model to highlight how flow processes couple to seismic radiation. Likewise, connections to actual seismic observations will require Green's functions that account for the location-specific elastic structure around a volcano, rather than the idealized structure used here.

4.1 Conduit flow model

Here we describe the unsteady conduit flow model used in our examples and show a representative eruption history. This is step I in the workflow stated in section 2.

We simulate conduit flow by simultaneously solving the governing equations for co-moving, two-phase magma with a common pressure in a vertical, rigid-walled cylindrical conduit. The momentum and mass balances are given by equations (7) and (8), respectively. Parameter choices and initial conditions are selected for idealized, short-duration vulcanian eruptions initiated by rupture of a plug that seals the conduit and allows for overpressure development beneath it.

Table 1. Parameter values used in example simulation in Section 4.

Symbol	Description	Numerical value
g	gravitational acceleration	9.8 m/s ²
f_0	Darcy-Weisbach friction factor	0.01
μ	magma viscosity	10 ⁶ Pa s
ϕ_0	critical gas volume fraction	0.8
t_{ex}	exsolution timescale	1 s
k	fragmentation transition sharpness	60
S_m	solubility constant	4×10^{-6} Pa ^{1/2}
n_0	total gas mass fraction	0.01
R_G	specific gas constant	461 J/kgK
T	mixture temperature	900 K
β_0	liquid compressibility	10 ⁻¹⁰ Pa ⁻¹
β_{ch}	chamber compressibility	2×10^{-10} Pa ⁻¹
$\rho_{l,0}$	liquid density	2600 kg/m ³
p_0	exsolution pressure	n_0^2/S_m^2
τ_p	plug traction amplitude	3×10^7 Pa
L_{plug}	plug traction width	173 m
z_{plug}	plug depth	250 m
t_{dur}	rupture duration	1 s
t_{rup}	time of rupture	10 s
V_0	chamber volume	10 ⁵ m ³
R	conduit radius	30 m
L	conduit length	1 km

The wall shear stress, τ , is written as the sum of the plug shear resistance, τ_{plug} , and drag from upward magma flow, τ_{drag} . The drag transitions from laminar to turbulent upon fragmentation, which we idealize as

$$\tau_{drag} = \frac{f_0 \rho v^2}{8} + \frac{8\mu v}{R} \frac{1}{1 + e^{k(\phi - \phi_0)}}, \quad (40)$$

where f_0 is the Darcy-Weisbach friction factor for turbulent flow, μ is magma viscosity, ϕ is gas volume fraction, and ϕ_0 is the critical volume fraction for fragmentation. We have smoothed the fragmentation process, specifically the transition from laminar to turbulent drag, using a logistic function in ϕ , centered around ϕ_0 and with the parameter k determining the sharpness of the fragmentation transition (Figure 2). The plug resistance model is described later.

The top pressure boundary condition is atmospheric pressure, $p(0, t) = p_{atm} = 10^5$ Pa, when the exit velocity is subsonic; otherwise, the flow is choked. The conduit is connected at its base to the lumped parameter chamber model given by equations (34) and (35).

The magma, a mixture of liquid melt and gas, obeys the mixture equation of state (Wilson & Head III, 1981)

$$\frac{1}{\rho} = \frac{n}{\rho_g} + \frac{1-n}{\rho_l}, \quad \rho_g = \frac{p}{R_G T}, \quad \rho_l = \rho_{l,0} (1 - \beta_0(p - p_0)) \quad (41)$$

where n is the mass fraction of exsolved gas, ρ_g is gas phase density determined by the ideal gas law, and ρ_l is liquid melt density, given by a linearized equation of state in which $\rho_{l,0}$, β_0 , and p_0 are the reference liquid density, compressibility, and reference pressure, respectively.

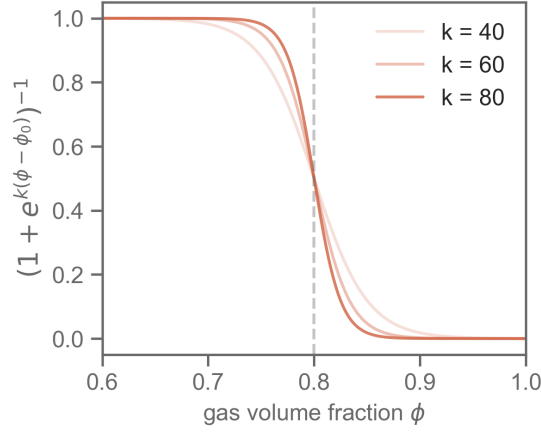


Figure 2. Fragmentation transition function in equation (40) that smoothly eliminates laminar drag as gas volume fraction increases above a fragmentation threshold (ϕ_0 , marked by the vertical dashed line). The parameter k determines the sharpness of the transition, with larger k creating a sharper transition.

Gas exsolution is captured through a simple evolution equation for the gas mass fraction n (Woods, 1995):

$$\frac{\partial n}{\partial t} + v \frac{\partial n}{\partial z} = - \frac{n - n_{eq}(p)}{t_{ex}}. \quad (42)$$

The left side is the material derivative of n , and the right side is the gas exsolution rate. We determine this rate by comparing the current gas mass fraction to the pressure-dependent equilibrium value $n_{eq}(p)$ and prescribing an exsolution timescale t_{ex} over which n approaches that value. The equilibrium gas mass fraction at a particular pressure is given by Henry's solubility law:

$$n_{eq}(p) = \max(n_0 - S_m p^m, 0) \quad (43)$$

where n_0 is total volatile mass fraction, S_m is the solubility constant for a particular volatile species, and m is the empirically determined exponent for that volatile species.

As mentioned earlier, we account for resistive tractions from a plug, idealized as

$$\tau_{plug} = \tau_p e^{-(z - z_{plug})^2 / (2L_{plug}^2)}, \quad (44)$$

where τ_p is the maximum plug traction, z_{plug} is the center of the plug, and L_{plug} determines its depth extent. The net force provided by the plug is

$$F_{plug} = \int_{-L}^0 2\pi R \tau_{plug} dz = (2\pi)^{3/2} R L_{plug} \tau_p. \quad (45)$$

The governing equations are solved, assuming $v = 0$ and $n = n_{eq}(p)$, for the initial pressure (Figure 3) by integrating downward from $z = 0$ where pressure equals atmospheric. The initial chamber pressure is set equal to the initial pressure at the bottom of the conduit. The eruption is initiated by smoothly reducing τ_{plug} to zero over rupture duration t_{dur} at time of rupture t_{rup} using a logistic function, $[1 + e^{(t - t_{rup})/t_{dur}}]^{-1}$.

The governing equations are written in conservation form (with dependent variables ρ , ρn , and ρu) and spatially discretized using high-order summation by parts (SBP) finite differences (Kreiss & Scherer, 1974). Boundary conditions are enforced weakly using the simultaneous approximation term (SAT) technique (Carpenter et al., 1994; Del

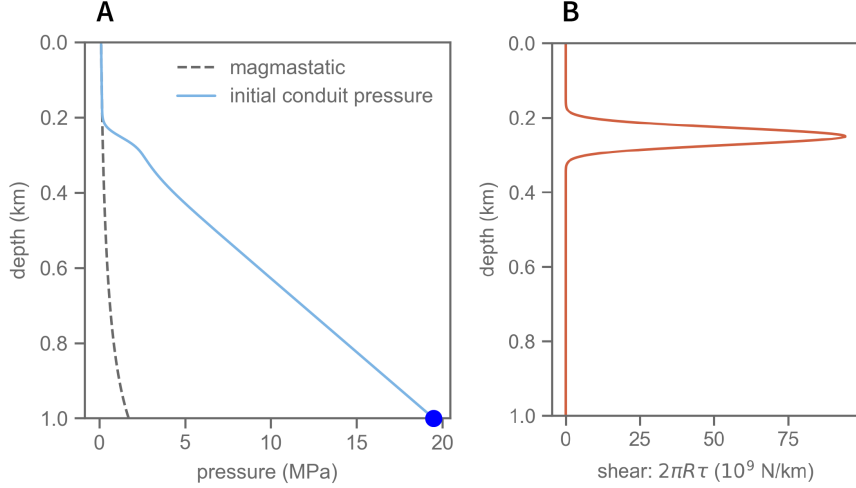


Figure 3. Initial pressure and shear traction along the conduit for an eruption initiated by plug rupture. **A)** Overpressure has developed below the plug, reaching almost 20 MPa above magmastatic pressure at the chamber. Dark blue dot indicates initial magma chamber pressure, which is the same as the pressure at the bottom of the conduit. **B)** Shear traction from the plug.

Rey Fernández et al., 2014). Specifically, we follow the approach in (Watson et al., 2019), which imposes boundary conditions on characteristic variables entering the domain from the boundary. The method can be proven to be energy stable for the frozen coefficient (linearized) problem. To increase robustness for the nonlinear problem, we add high-order artificial dissipation (Mattsson, 2017).

Time stepping is done using an adaptive Runge–Kutta method. In all simulations, we use a uniform grid spacing of 0.98 m, chosen to adequately resolve the (smoothed) fragmentation front without introducing artificial oscillations. The exception to this is our later study of intermittent fragmentation, in which we purposefully sharpen the fragmentation to produce discretization-dependent effects. The rationale for this is discussed later.

Table 1 lists parameter values for the example simulation in this section. The parameter values are similar to those chosen in many class conduit flow models (Wilson et al., 1980; Woods, 1995) and are reasonably representative of a moderately viscous magma (e.g., dacite). The gas content ($n_0 = 0.01$) is at the lower end of possible values, which we purposefully selected so that there is no exsolved gas in the magma beneath the plug at the onset of the eruption. This allows us to use the equilibrium solubility model when setting the initial conditions for the simulation, thereby avoiding the need to account for effects of outgassing prior to the eruption.

The results are shown in Figure 4 for an eruption in a conduit with of length 1 km and radius 30 m connected to a magma chamber with volume of 10^5 m^3 . A spherical chamber of this volume has radius approximately equal to the conduit radius. Rupture of the plug reduces the restraining tractions, and the overpressure beneath the plug then accelerates the magma upward. This upward flow depressurizes the conduit, with the leading edge of the decompression front traveling down the conduit at the sound speed in the magma. Magma exits the vent at the sound speed (choked flow) in the early parts of the eruption for a few hundred seconds, then slows to subsonic exit velocities. Once the decompression front reaches the chamber, the chamber begins to depressurize as mass

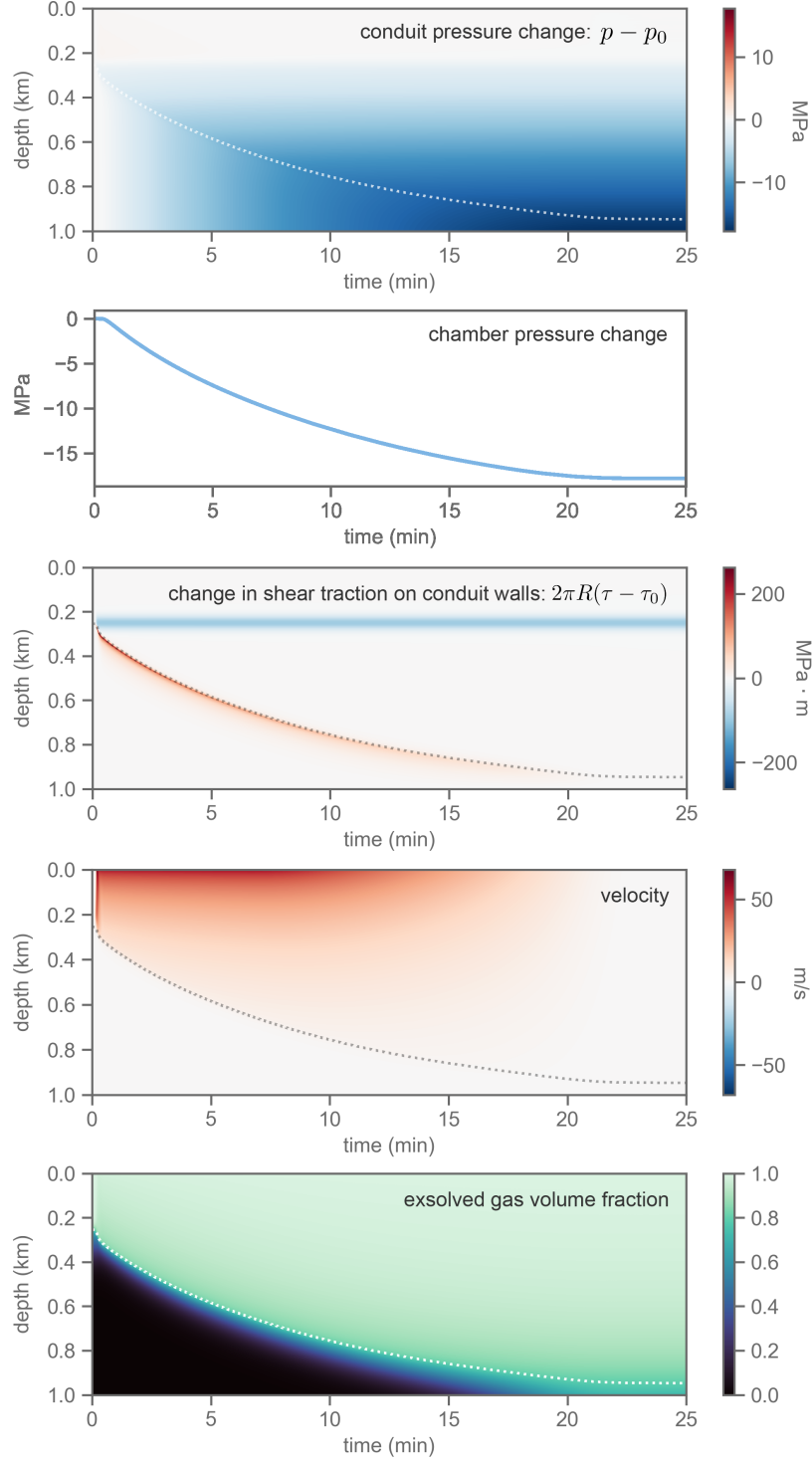


Figure 4. Simulation results for eruption initiated by plug rupture with initial conditions shown in Figure 3. Rupture initiates upward acceleration of the magma and depressurization of the conduit and chamber. Dashed lines track the descent of the fragmentation front, also highlighted by the high upward drag from acceleration of magma just below the front. The persistent region of reduced shear traction around 250 m depth marks the plug location prior to rupture.

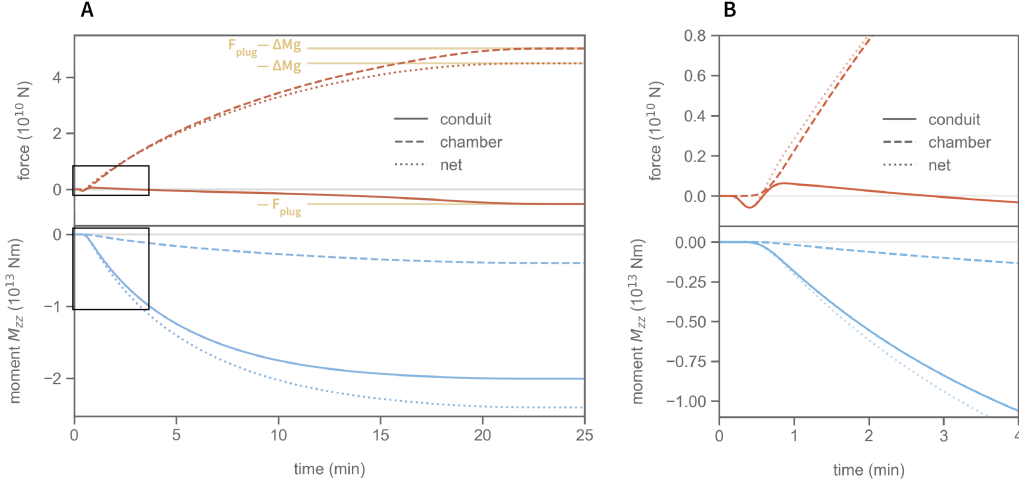


Figure 5. Point-source force and moment histories for the simulated eruption triggered by plug rupture. **A:** For entire eruption. **B:** The first 4 minutes (marked by black boxes in **A**). Depressurization of the conduit dominates the moment history all throughout the eruption. The force history illustrates a shift in dominance from the conduit force early in the eruption to chamber force for the duration of the eruption. Note that only the M_{zz} component of the moment tensor is plotted; other components' histories will be scaled by a ratio of elastic moduli.

flows from the chamber into the conduit. The rate of chamber decompression depends on the storage capacity of the chamber, which is determined by the compressibility of the magma, the elastic compliance of the chamber, and the chamber volume. As the magma decompresses, it becomes saturated with volatiles and gas exsolves from the melt, increasing the gas volume fraction. Once the gas volume fraction exceeds a threshold value, the magma fragments and friction between the magma and the wall is drastically reduced as it transitions into a turbulent, gas-continuous flow. Figure 4 shows high upward tractions on the conduit walls just below the fragmentation front, as magma still within the high-drag laminar flow regime is accelerated upward. There is also a region of downward shear traction change centered at 250 m depth that persists for the rest of the simulation; this is the region where the plug was located prior to rupture. The eruption ends gradually as depressurization of the conduit and chamber brings the system toward magmatic balance.

4.2 Force and moment histories

Here we use the source representation to convert the eruption history to seismic force and moment. This is step II in the workflow stated in section 2. The conduit contributions to force and moment for a finite source are proportional to the shear traction and pressure change distributions shown in Figure 4. For the point source representation for the conduit contribution, moment and force distributions – converted from pressure and shear traction changes using equations (1) and (2) respectively – are integrated along the length of the conduit to get point moment tensor and force histories. The chamber moment contribution is proportional to changes in chamber pressure (3), while the chamber force contribution arises from conduit-chamber momentum exchange (including the change in conduit magma weight) and the change in chamber magma weight (4). Point moment and force histories are shown in Figure 5.

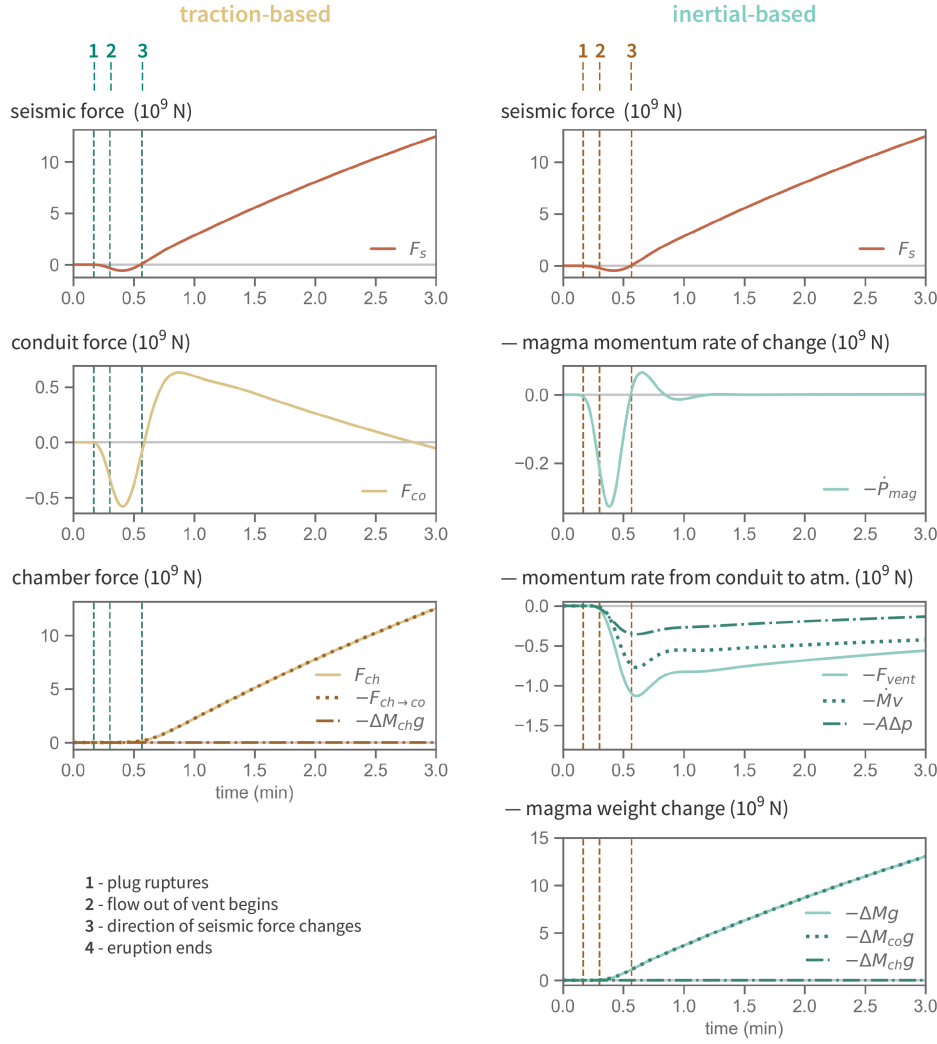


Figure 6. Seismic force history (positive up) and its decomposition into contributions for the traction-based (left column) and inertial-based (right column) representations for the eruption shown in Figure 4. Four transition points are marked: 1) eruption is initiated by plug rupture, 2) flow out of the conduit begins, 3) the seismic force switches direction from downward to upward, 4) the eruption stops when magmastatic balance is reached (see long time limit in Figure 5). For the traction-based representation, $F_s = F_{co} + F_{ch}$, where F_{co} is the integrated shear traction change on the conduit walls and $F_{ch} = -F_{ch \rightarrow co} - \Delta M_{ch}g$, the sum of minus the rate of momentum transfer from the chamber to conduit (calculated as $-A\Delta p_{ch}$) and minus the chamber weight change. For the inertial-based representation, $F_s = -\dot{P} - F_{vent} - \Delta Mg$, where \dot{P} is the rate of change of subsurface magma momentum, F_{vent} is the rate of momentum transfer to the atmosphere, and ΔMg is the change in weight of the subsurface magma. Note that $F_{vent} = \dot{M}v + A\Delta p$ at the vent, where $\dot{M} = \rho v A$ is the mass eruption rate. The commonly used approximation, $F_s \approx -\dot{M}v$, is not justified for this eruption. Figure 5 shows the force history for an additional 22 min, during which F_s continues to increase to its static value as the subsurface magma weight decreases.

Next we decompose and interpret the seismic force history shown in Figure 5, using both the traction-based and inertial-based representations, in Figure 6. We mark different transition points of the eruption event: 1) eruption initiation, 2) magma beginning to exit the conduit vent, 3) direction change of seismic force, and 4) eruption cessation (most clearly seen in Figure 5 because Figure 6 is focused on the early part of the eruption).

First, we discuss the traction-based representation of the seismic force, F_s . The eruption begins with rupture of the plug (transition 1) and seismic force contributions from the conduit (F_{co}). There is no contribution from the chamber (F_{ch}), as significant flow has not yet begun at depth. Prior to rupture, the magma pushes upward on the surrounding solid, such that removal of the restraining shear tractions results in a net downward contribution to the seismic force on the solid Earth equal to $-F_{plug}$. However, this downward force is partially canceled by upward drag on the conduit walls as magma flows upward, such that the maximum force in this phase of the eruption, while downward, is much smaller in magnitude than F_{plug} . As the eruption progresses and magma begins to exit the vent (transition 2), already-moving melt continues to be accelerated and flow is initiated at greater depths, both of which increase upward drag on the conduit walls. Eventually, this upward drag overcomes the initial loss of restraining tractions from the plug, leading to F_{co} and thus F_s changing direction to become upward (transition 3). The next phase of the eruption features substantial depressurization and loss of mass (and weight) from the conduit and chamber, such that F_{ch} contributes an upward force to F_s . Note that the weight reduction within the conduit appears through the $-A\Delta p_{ch}$ term in F_{ch} . As the ascent rate of magma in the conduit decreases, the upward drag decreases until it is no longer larger than $-F_{plug}$. Thus the conduit force becomes downward again, with $F_{co} \rightarrow -F_{plug}$ as the eruption wanes. In this phase of the eruption, the chamber contribution, F_{ch} , dominates the conduit contribution, F_{co} , for the remainder of the eruption. At the end of the eruption, magma returns to rest and magmastatic balance is achieved (transition 4, corresponding to the long time limit shown in Figure 5). The seismic force is upward and is equal to minus the change in magma weight: $F_s = -\Delta Mg$. This can be understood from force equilibrium concepts as follows. The expression for F_{ch} is given by equation (37), in which the first term (minus the change in force at the base of the conduit supporting the overlying magma column, $A\Delta p_{ch}$) must equal the weight change of conduit magma minus the plug force: $A\Delta p_{ch} = \Delta M_{co}g - F_{plug}$, and the second term is minus the weight change of chamber magma, $-\Delta M_{ch}g$. Thus, $F_{ch} = -\Delta M_{co}g + F_{plug} - \Delta M_{ch}g$, which is upward (less upward force required to support the magma, which means less downward force on the solid Earth). The conduit force contribution, in this equilibrium limit, is simply $F_{co} = -F_{plug}$ because there is no drag. Thus, $F_s = F_{co} + F_{ch} = -\Delta Mg$, which is upward.

Next we discuss the seismic force history in the inertial-based representation. The magma initially starts from rest with zero momentum. Rupture of the plug (transition 1) removes restraining tractions, accelerating the conduit magma and increasing its upward momentum. Momentum conservation requires the transfer of downward momentum to the solid Earth, reflected in the downward F_s . Magma has not yet exited through the vent, so there is no momentum exchange with the atmosphere and no loss in weight. Once the accelerating magma reaches the vent (transition 2), upward momentum is transferred to the atmosphere and the rate of momentum increase within the conduit begins to slow, again corresponding to downward momentum imparted to the solid Earth. As mass is erupted through the vent, the weight of magma remaining in the subsurface conduit-chamber system decreases, providing an upward contribution to F_s . Eventually, the reduced weight overcomes the contribution from the changing magma momentum and momentum transfer rate to the atmosphere, and the imparted momentum to the solid Earth and therefore F_s change direction (transition 3). Upward momentum continues to be exchanged with the atmosphere over the remainder of the eruption, but at a rate that decreases as the eruption wanes. Likewise decreasing is the rate of change of conduit magma

momentum. As these contributions to F_s diminish, the largest contribution during this period comes from the weight change of subsurface magma as mass is erupted into the atmosphere. At the end of the eruption (transition 4, corresponding to the long time limit shown in Figure 5), there is no longer any change in magma momentum and no momentum exchange with the atmosphere, as magma is now at rest. The final static value of the seismic force is the total weight of erupted magma, $F_s = -\Delta Mg$.

The moment tensor histories (Figure 5) capture the depressurization of the conduit and the chamber. For the particular set of parameters chosen for this simulation, the moment tensor contribution from the conduit dominates over the chamber contribution because the conduit volume is greater than chamber volume by an order of magnitude; this balance will shift as chamber size increases relative to conduit size. This is explored later in our study through a parameter-space study varying the chamber volume.

Having discussed the relation between the eruptive history and the seismic force and moment tensor histories, we next turn to the expression of eruptive processes in seismograms. This adds an additional layer of complexity in the interpretation process, as contributions from the force and moment are superimposed to produce the overall seismogram.

4.3 Synthetic seismograms

Here we produce synthetic seismograms from the force and moment histories of the previous section. This is step III in the workflow stated in section 2. We do this for both the finite source and point source representations, discussing when the point source approximation is appropriate and highlighting the potential benefits of near-source receivers that can resolve finite source effects to better constrain the eruptive processes.

For simplicity, we use homogeneous half-space Green’s functions for a solid having density 2700 kg/m^3 , P-wave speed 3.464 km/s , and S-wave speed 2 km/s . Green’s functions are numerically generated using the FK method and associated code (Zhu & Rivera, 2002). We treat the conduit and the chamber as two separate sources that are added together to get the final synthetic seismogram. The chamber is represented as a point source at a depth of 1.028 km (the center of a spherical chamber of the given 10^5 m^3 volume) for both the point-source and extended source calculations. In the point-source representation, we calculate the conduit contribution by first integrating the moment (1) and force (2) contributions over the length of the conduit to get source histories for a single source at depth 500 m (the midpoint of the conduit). In the finite-source calculation, we first calculate the seismogram contribution from each point along the conduit by treating each simulation spatial grid point as a point source at that depth. For each simulation grid point, we get moment and force histories for that position in the conduit and convolve those with the Green’s functions specific to that source depth. We then add up contributions from all grid points in the conduit. This allows us to account for the travel-time difference between different parts of the conduit, as well as the change in source-receiver orientation that leads to different radiation patterns at the receiver position. We encountered numerical inaccuracies in the Green’s functions for sources close to the surface. To mitigate this issue, we used the Green’s function for a source depth of 100 m for contributions in the uppermost 100 m of the conduit. Because this scale is much shorter than the wavelengths of seismic waves and static deformation, the error in this approximation is negligible.

Figure 7 shows the synthetic seismograms for our example simulation at a receiver 3 km from the vent. The displacement seismograms from the force and moment contributions show similar features to the source histories shown in Figure 5. The vertical component is dominated by the force contribution throughout the eruption. Within the first minute after the eruption onset, the ground first moves downward and inward in response

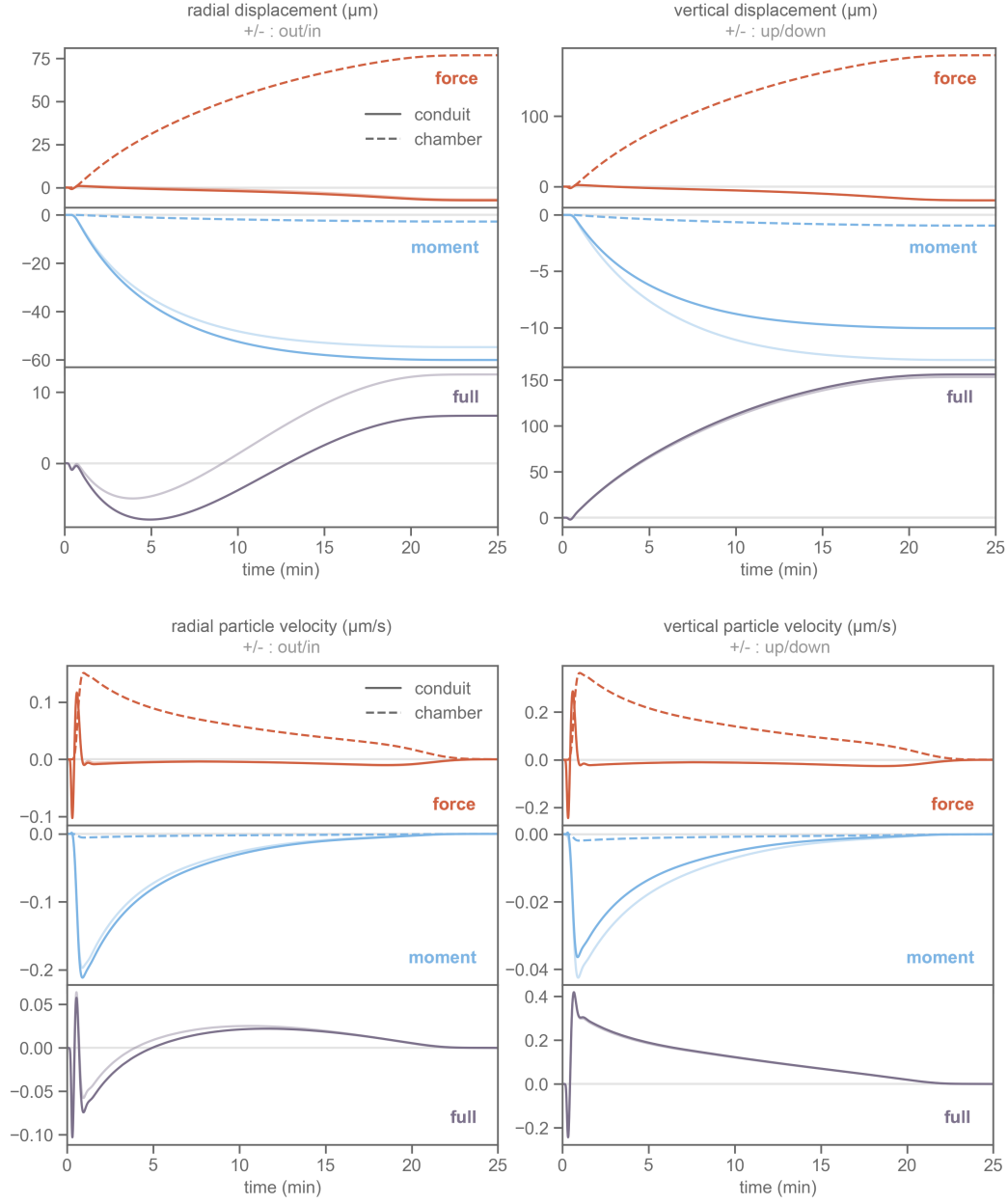


Figure 7. Synthetic displacement and velocity seismograms for a receiver located 3 km from the vent. The full waveform combines all contributions from the conduit and chamber. Faint lines are the extended-source calculation, while dark lines are point-source. For the first minute after the eruption onset, the conduit force contributions dominate, creating radially inward and downward motions. Thereafter, the displacements evolve toward their static values, radially outward and upward. The force, specifically the weight change, produces outward and upward displacement, whereas the moment, from depressurization, is of opposite sign. These contributions are comparable on the radial component, with the force contribution being slightly larger in the static limit. The vertical component is dominated by the force.

to the downward seismic force from the loss of restraining tractions on the conduit walls. Next it moves upward, in response to the upward drag of the accelerating magma at and below the fragmentation front. This is followed by downward motion again from the depressurization moment source. After the seismic force direction changes (transition 3), the chamber force, specifically the upward seismic force from the reduction in weight, dominates for the remainder of the eruption to cause upward and outward displacement. The radial seismograms are more complex. The small inward motion from the downward force is followed by a larger inward motion from the depressurization moment source. However, after ~ 10 min, the displacement direction reverses to outward as the upward seismic force from the weight change increases, eventually counteracting the inward motion from the depressurization moment source. The static displacements are dominated by the upward seismic force from the weight change on the vertical component, whereas the radial component has equally important contributions from depressurization (inward, moment) and the weight change (outward, force), with the weight change contribution being slightly larger.

Note that any difference between the finite- and point-source calculations arises in the conduit contribution, since we treat the chamber as a point source in both representations. Therefore in the final vertical waveform, there appears to be little difference between the two calculations because the chamber force dominates the vertical signal for the majority of the eruption. In the radial signal, the waveform shape looks consistent between the two calculations – capturing the same shift in dominant contributions – but the timing of the transition is shifted, reflecting the overestimation of the displacement and particle velocity from the conduit moment in the point-source calculation.

Next we explore how the seismograms change with distance from the vent (Figures 8 and 9). The discussion to follow focuses first on displacements at times greater than approximately minute. We then return to the first minute of the eruption, where eruptive processes are most clearly identified in the velocity seismograms. Returning to the longer time scales, the vertical displacements at all distances are upward, reflecting the weight change contribution to the seismic force. The depressurization moment source contributes at distances out to a few km, providing a downward displacement that reduces the upward displacement from the reduction in weight, but this moment contribution becomes negligible in comparison to the force contribution at greater distances. The radial displacements are more complex, with substantial changes in the waveform shape and even displacement direction as receiver distance increases. Again we focus on times later than the initial minute of eruption. At 1 km from the vent, the radial displacement is inward for all times, primarily reflecting depressurization of the conduit. As the receiver distance increases, the force contribution from the reduction in weight becomes increasingly more important, particularly toward the end of the eruption. At sufficiently large receiver distances, the weight change force is the dominant contribution throughout the seismogram, including in the static upward displacement.

We also note that differences between the point- and finite-source seismograms are most pronounced for receivers close to the vent, as expected. The point-source calculation overestimates the velocity/displacements, especially later in time. This is because substantial depressurization in the later part of the eruption occurs at depths below the source depth used for the point-source calculation (see Figure 4) and thus farther from the receiver. However, we note that the general eruption features are captured in both point- and finite-source seismograms, so differences in interpretation using a point-source approximation would only be quantitative, rather than qualitative.

Eruptive processes in the first minute or two are most clearly expressed in the velocity seismograms (Figure 9). At all distances, we see an initial downward and inward velocity from the loss of restraining tractions when the plug ruptures. The shift to later arrival times of this feature with increasing receiver distance is a consequence of the increased wave travel time. The vertical velocity then switches to upward, reflecting the

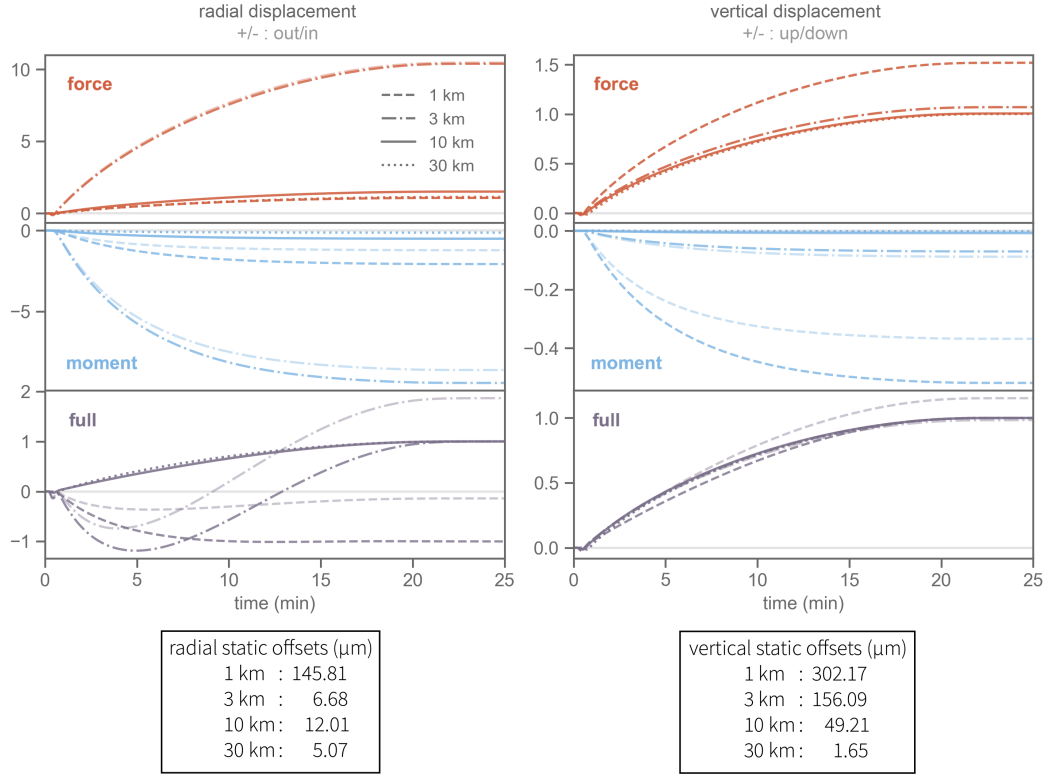


Figure 8. Scaled synthetic displacement seismograms at four receiver distances: 1 km, 3 km, 10 km, 30 km. Conduit and chamber contributions are combined. For each receiver distance, all of the contributing waveforms are scaled by the final point-source full-waveform static displacements noted in the tables at bottom of figure. Faint lines are extended-source and dark lines are point-source. Receiver positions closer to the conduit exhibit different dominant contributions to radial displacement, changing the waveform significantly. Beyond a certain distance, the waveform features have little dependence on receiver position.

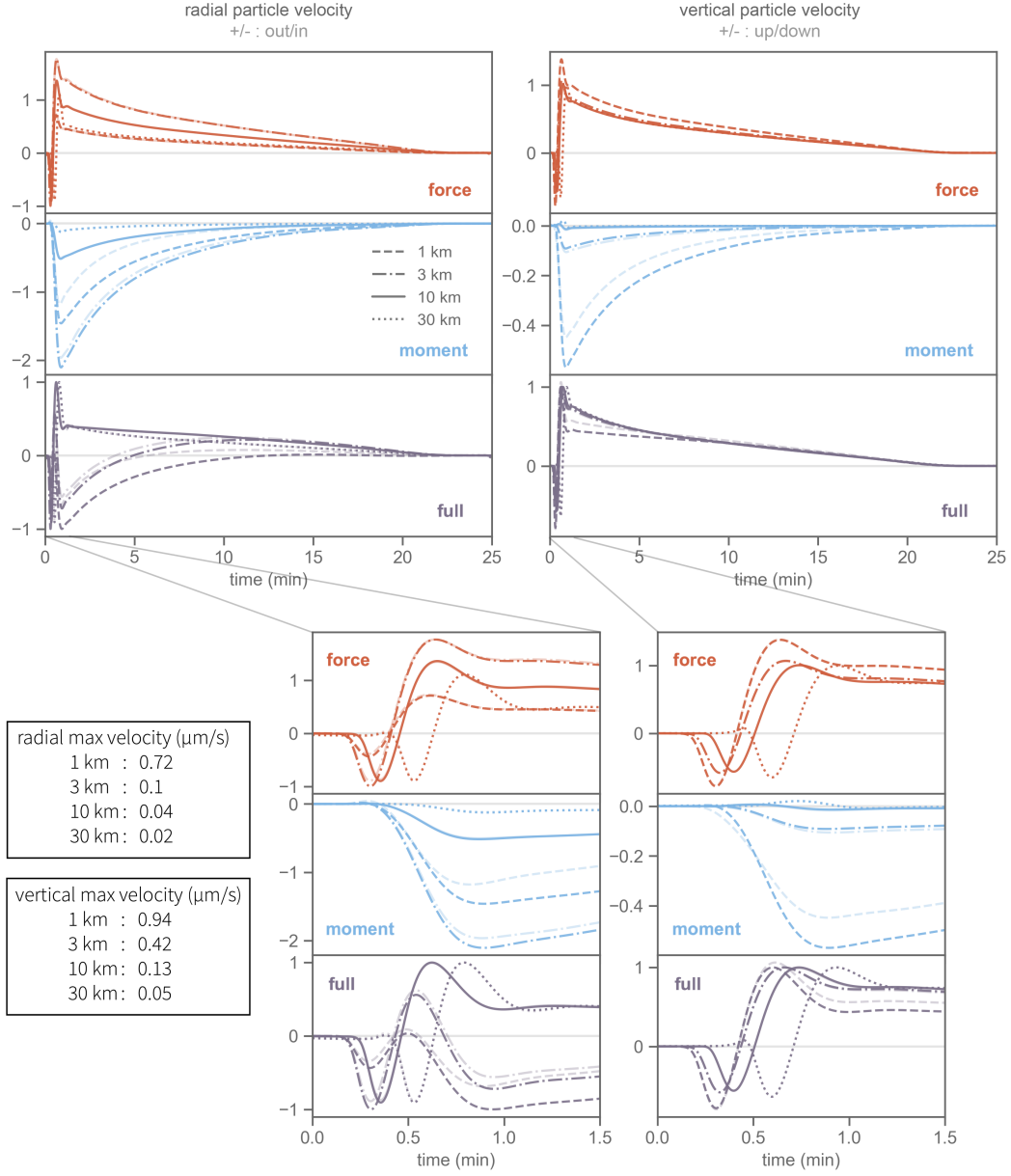


Figure 9. Scaled synthetic velocity seismograms calculated for four different receiver distances: 1 km, 3 km, 10 km, 30 km. Conduit and chamber contributions are combined. For each receiver distance, all of the contributing waveforms are scaled by the magnitude of the maximum particle velocities in the point-source full-waveform noted in the tables at bottom of figure. Faint lines are extended-source and dark lines are point-source. Different receiver position can highlight different contributions through changes in waveform features.

weight change force contribution. The radial velocity, initially inward from the plug rupture, switches to outward at more distant receivers from the weight change. At close distances, the response is a more complex superposition of inward velocity from depressurization and outward velocity from the weight change. This example demonstrates the importance of having receivers at different distances to constrain eruptive source processes.

5 Interpreting force history through parameter exploration

We now use the new workflow to investigate how eruptive processes, which we alter by changing select model parameters, are reflected in the force and moment histories and also in the seismograms. In particular, we focus on the sharpness of the fragmentation transition and on the chamber volume. Each simulated eruption starts with the same initial pressure and stress conditions along the conduit and chamber and the same triggering event of the plug rupture.

5.1 Fragmentation transition

Fragmentation is modeled through the drag term in the conduit momentum balance (7), which is reduced as the volume fraction fragmentation condition is met. This smooth transition is given in equation (40) and shown in Figure 2. Here we vary the parameter k , which sharpens the transition as it is increased.

Figure 10 shows that the fragmentation front descends through the conduit more quickly as the fragmentation transition is sharpened. Increasing the sharpness of the fragmentation transition means that the reduction in friction occurs over a smaller range of gas volume fractions. This means that there will be a smaller depth range over which friction is being reduced, leading to a sharper stress gradient. Therefore, magma just below the fragmentation front will be accelerated more for higher values of k , as indicated by the higher shear stress on the conduit walls just below the fragmentation front and the greater erupted mass rate (Figure 10). Faster acceleration of the magma also leads to faster decompression and thus volatile exsolution, causing the magma to fragment sooner. This leads to the faster descent of the fragmentation front through the conduit, faster depressurization of the conduit and chamber, and a larger eruptive mass rate that more quickly reduces the weight of the subsurface magma.

The changes in the eruption described above are reflected in the force and moment histories and seismograms (Figure 11). Sharper fragmentation, which leads to more rapid descent of the fragmentation front and associated upward acceleration of magma, is expressed in the increased amplitude of the initial downward-upward-downward motions in the first minute. The initial downward/inward motion is from the loss of restraining tractions as the plug ruptures, and the subsequent upward/outward motion is caused by upward drag from the accelerating magma just below fragmentation. The switch to downward motion comes from the depressurization moment contribution that temporarily overcomes the upward force contribution. The larger eruption rate from sharper fragmentation depressurizes the system and reduces the magma weight faster. These changes affect both the force and moment at later times, increasing the velocity amplitude on both components.

5.2 Chamber volume

We compare simulated eruptions with three different chamber volumes: $V_0 = 10^5 \text{ m}^3$, 10^8 m^3 , and 10^9 m^3 (Figure 12). Larger chambers have larger storage capacity and hence smaller pressure changes for the same magma mass removed from them. All simulations have the same initial pressure and restraining shear tractions along the conduit and in the chamber; therefore, the initial eruption process is identical. However, the slower

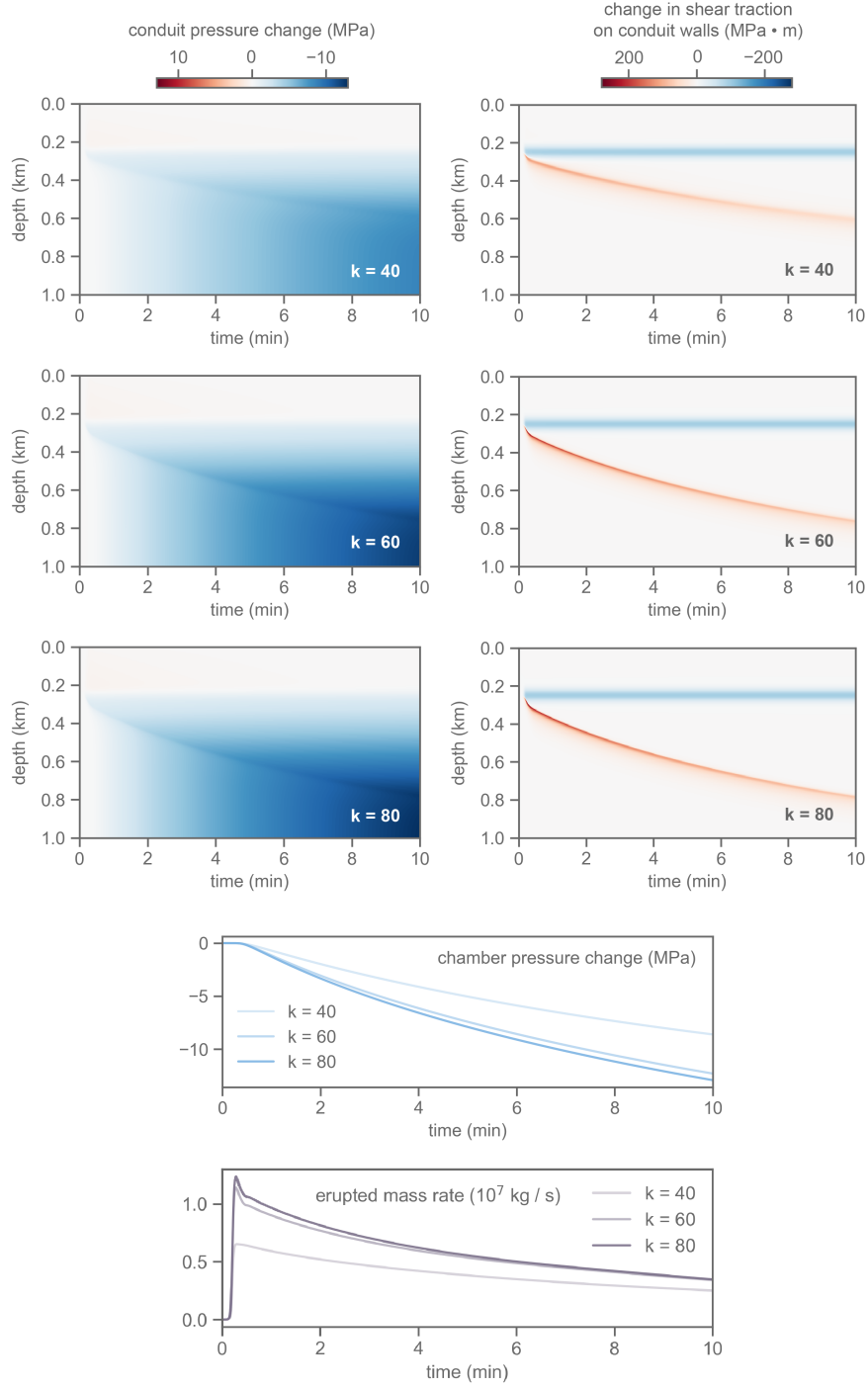


Figure 10. Simulation results for different fragmentation transitions: increasing k increases the sharpness of the transition. Initial pressure/shear traction conditions and parameter values (except k) are the same as example simulation in Section 4. Sharper fragmentation produces faster decompression and greater acceleration of magma just below the fragmentation front.

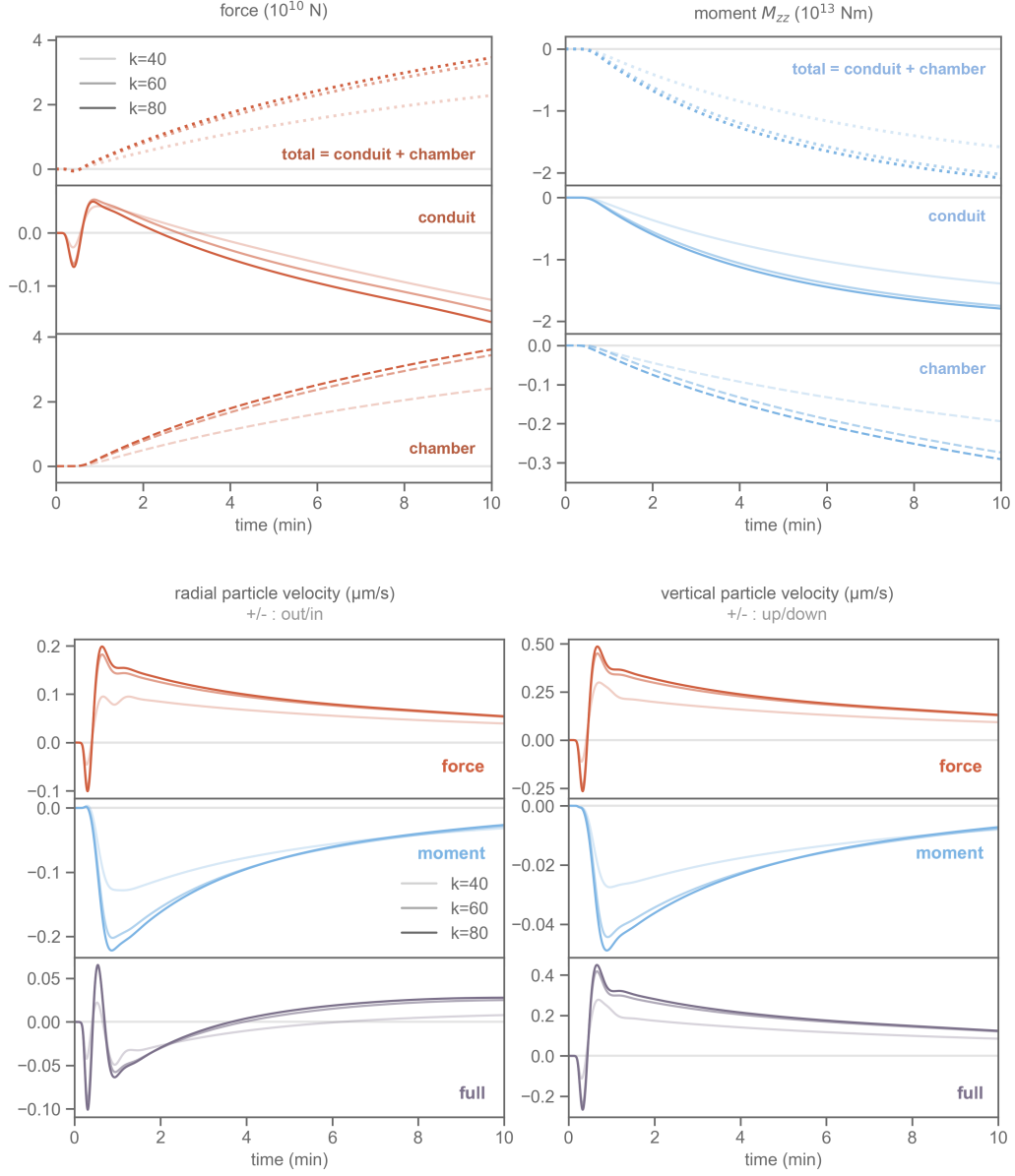


Figure 11. (top) Point-source force and moment histories and (bottom) velocity seismograms for different sharpness of fragmentation from eruption simulations shown in Figure 10. Sharper fragmentation increases the force-dominated contribution in the first minute of the seismograms and also produces larger amplitude upward/outward motions from more rapid loss of weight at later times.

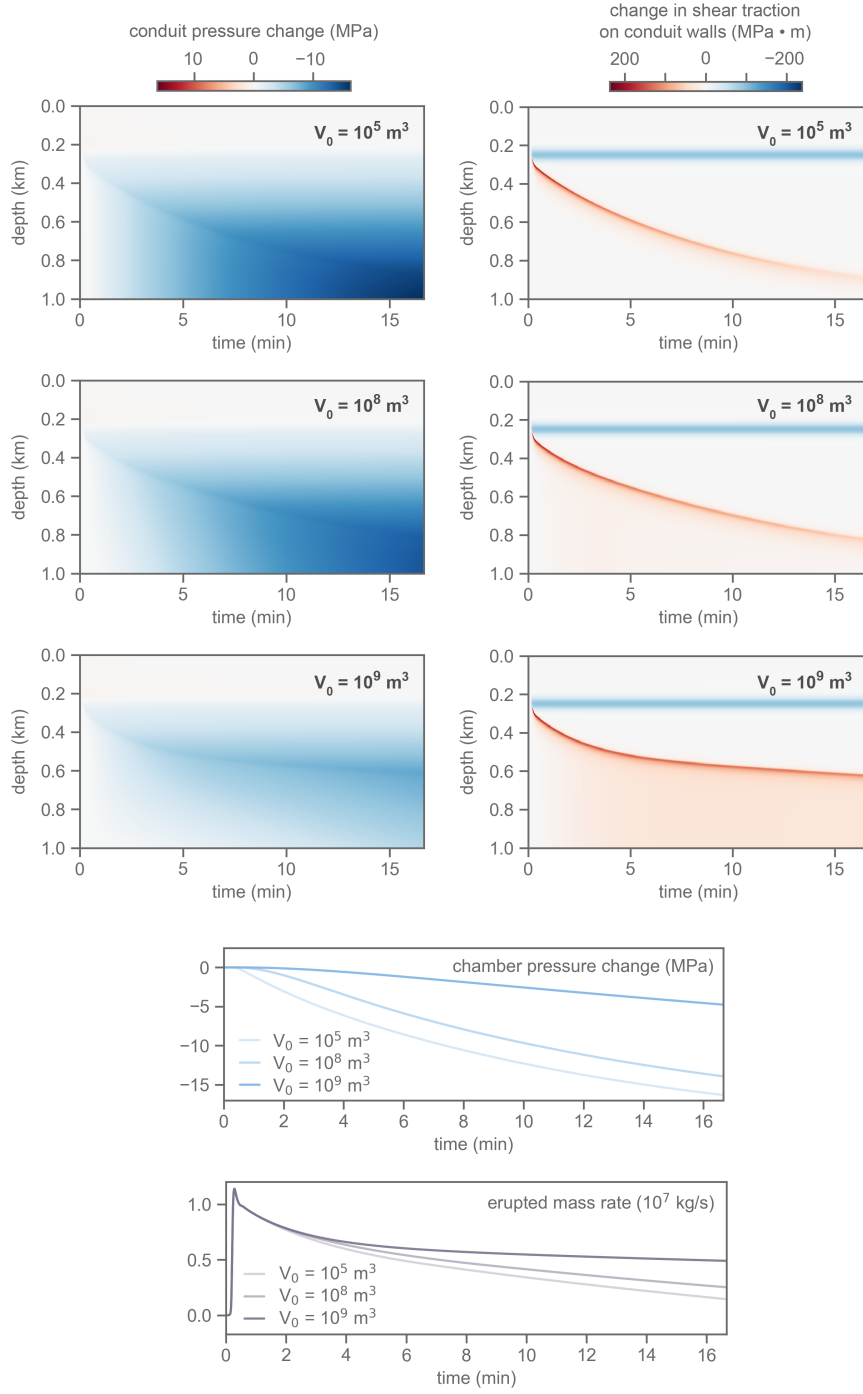


Figure 12. Simulation results for different chamber volumes, V_0 . Initial conditions and parameter values (except V_0) are the same as example simulation in Section 4. The larger storage capacity of high volume chambers slows the depressurization and return to magmastic balance. In addition to extending the eruption duration, this slow depressurization maintains a larger upward pressure gradient and hence larger particle velocities and more drag below the fragmentation front.

depressurization of larger chambers serves to maintain a greater pressure gradient and delays the return to magmastatic balance. This is evident in plots of the conduit and chamber pressure change. In addition, the fragmentation front descends more slowly for larger chambers because the higher pressures inhibit gas exsolution and expansion. The steeper pressure gradient also leads to more magma flow, both out of the vent (see erupted mass rate) and deeper in the conduit. The faster flow produces greater upward drag everywhere below the fragmentation front (see shear traction changes).

The force and moment histories and seismograms (Figure 13) capture the differences in eruption features. The chamber depressurization dominates the moment contributions as chamber volume becomes large compared to the conduit volume. Larger chambers also produce larger upward forces in the conduit from the upward drag of the ascending magma. While the conduit force ultimately becomes downward, with $F_{co} \rightarrow -F_{plug}$ as the eruption ends, the amplitude and duration of the upward conduit force phase increases with increasing chamber volume. That said, the upward force contribution from the weight change, which increases slightly as the chamber volume and eruption rate increase, is the dominant contribution to the net force.

Turning to the seismograms, we again see that the vertical force from plug rupture and upward drag in the conduit controls the seismic signal for the first minute after eruption onset. Then, when the chamber volume is larger than the conduit volume, the inward/downward motions from chamber depressurization dominate the seismograms. The force contribution from the weight change becomes negligible in comparison to this depressurization moment source, except for the smallest chamber volume studied here (which is the same as in previous examples in our study). The final static displacement will be a balance between the outward/upward static displacement from the loss of erupted magma weight (force) and the inward/downward displacement from the depressurization of the large chambers (moment). Thus it may be challenging or impossible to determine the weight change force contribution except for eruptions with small chamber contributions.

6 Intermittent fragmentation descent

As we increase the fragmentation parameter k , the length scale over which fragmentation occurs shortens. When this length scale becomes smaller than the grid spacing along the conduit, fragmentation occurs in discrete bursts as the fragmentation front passes each grid point. This manifests as the intermittent descent of the fragmentation front through the conduit. While this effect is numerical, and dependent on the spatial discretization, we speculate that similar intermittency occurs in actual eruptions as a consequence of heterogeneity in magma strength, bubble distributions, and related small-scale processes controlling fragmentation. Thus we utilize our underresolved simulations with intermittent fragmentation descent to examine how this is expressed in the force and moment histories and seismograms. Simulation results are shown in Figure 14 for initial conditions shown in Figure 3 with $k = 1500$ (though the specific value is irrelevant once it is sufficiently high).

As evident in Figure 15, intermittent fragmentation manifests as high frequency features in both the force and moment histories, though contributions to the seismogram are dominated by the force. As each point fragments, the restraining tractions at that point drop abruptly, creating a downward seismic force. Immediately after this, the parcel of newly fragmented magma is accelerated upwards, expanding the magma above fragmentation and creating a drop in pressure. The magma below fragmentation quickly accelerates, producing an upward force. Thus each fragmentation event is reflected in a two-sided down-up force cycle. This is similar to the force history from plug rupture, except at a smaller scale.

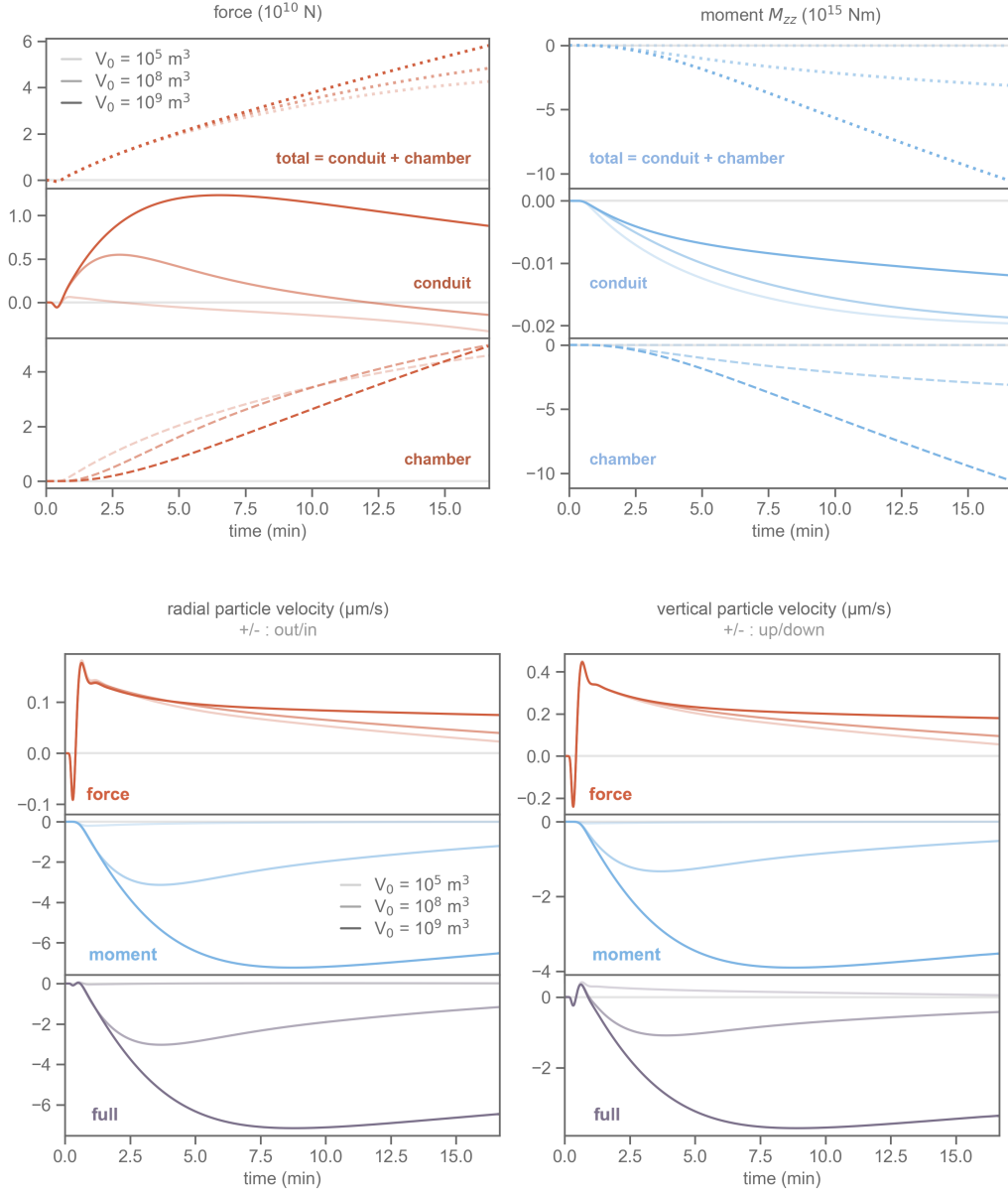


Figure 13. (top) Point-source force and moment histories and (bottom) velocity seismograms for different chamber volumes from eruption simulations shown in Figure 12. The eruption process is identical for the first minute or so. Later, the slower depressurization of the larger chambers leads to higher pressure gradients, faster flow, and higher upward drag that appears in the conduit force. The depressurization of the chamber dominates the moment histories as chamber volume becomes large compared with the conduit volume.

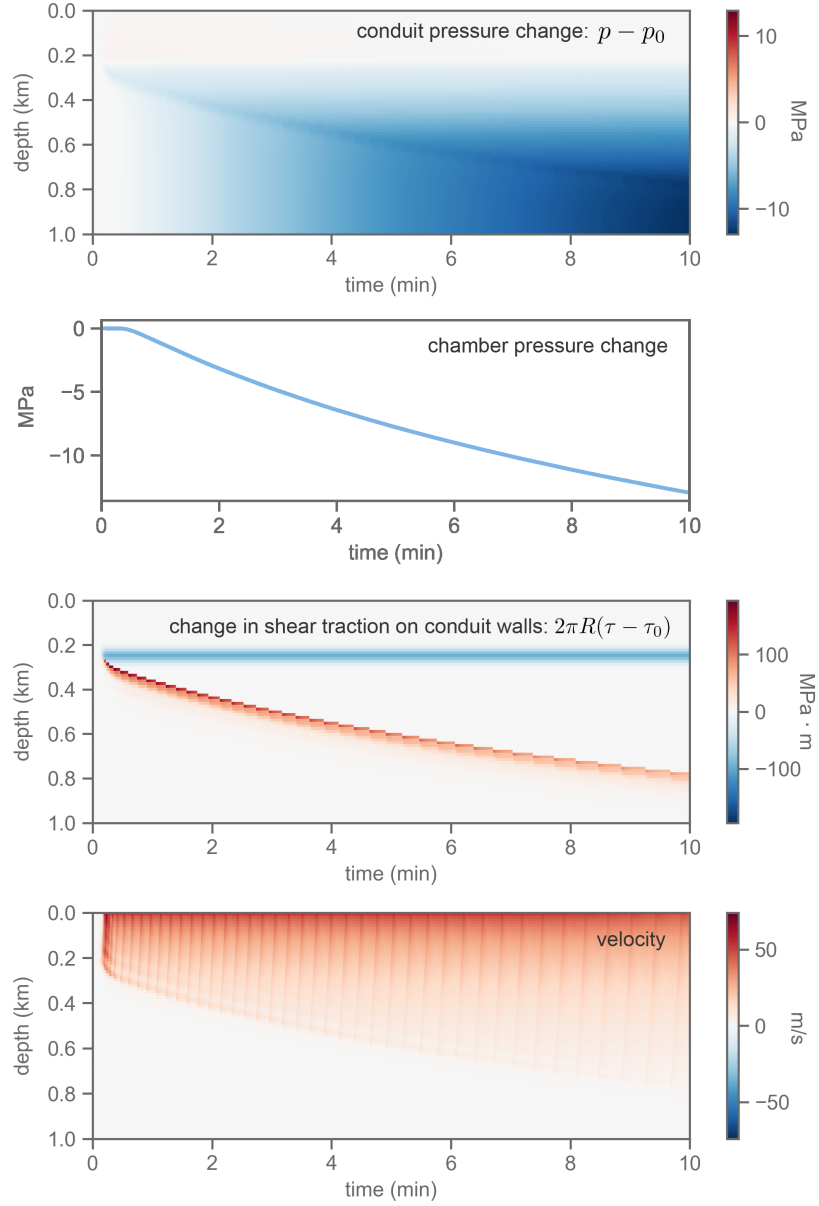


Figure 14. Simulation results exhibiting intermittent fragmentation descent from numerically underresolved sharp fragmentation ($k = 1500$, though the specific value is irrelevant once it is sufficiently high). Initial conditions and parameter values (except k) are the same as example simulation in Section 4. As parcels of magma fragment, impulsive acceleration of the magma triggers advected acoustic waves that propagate up to the vent.

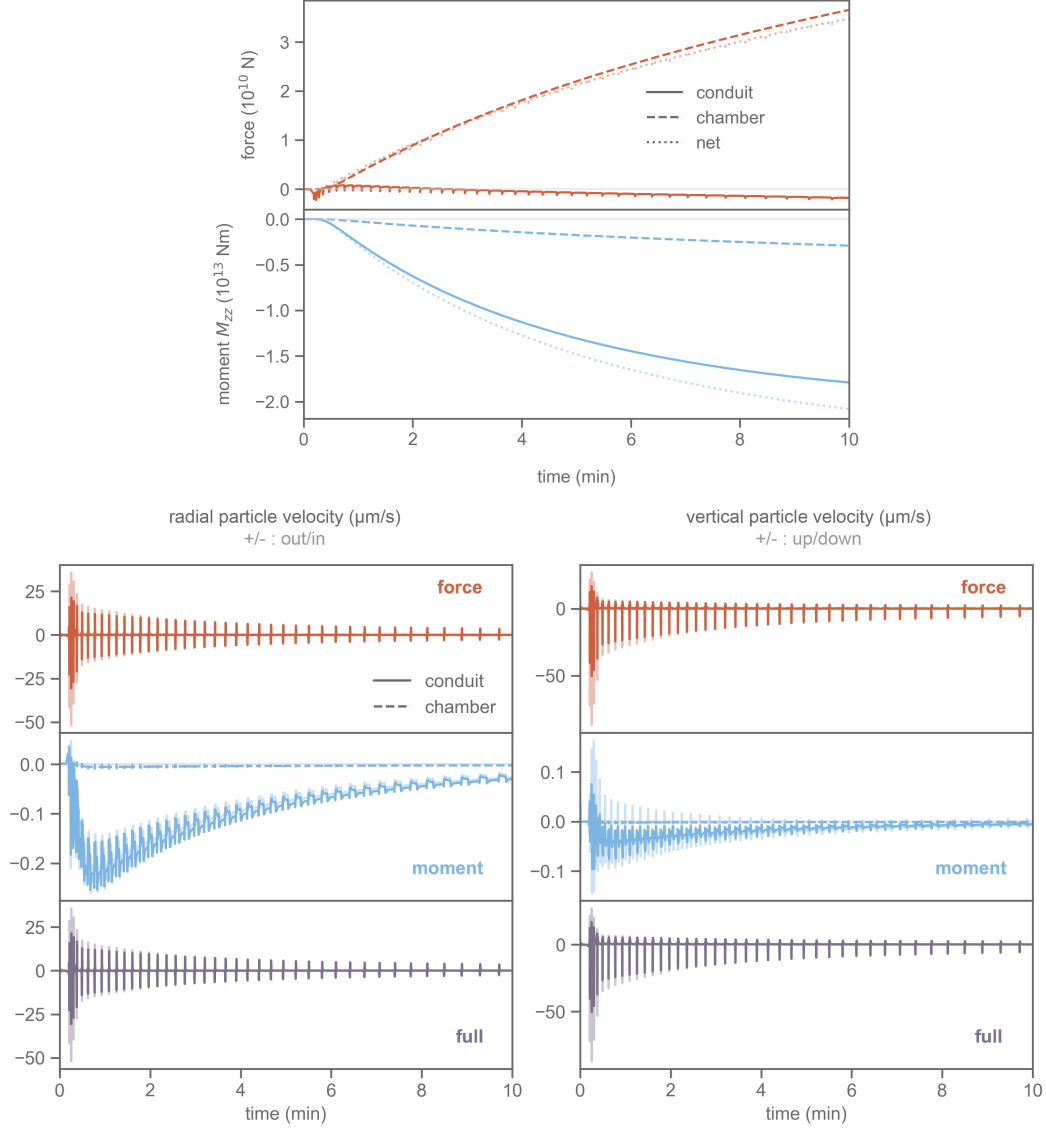


Figure 15. (top) Point-source force and moment histories and (bottom) velocity seismograms for intermittent fragmentation descent from eruption simulations shown in Figure 14. The conduit force captures the impulse from parcels of melt fragmenting.

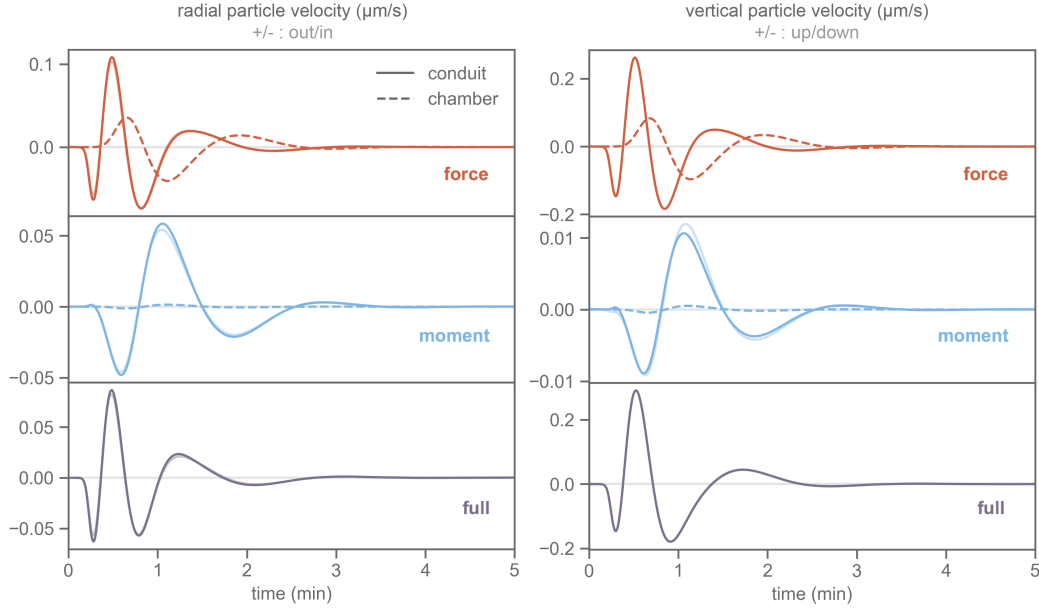


Figure 16. High-pass filtered synthetic velocity seismograms for receiver placed 3 km from conduit vent (shown in Figure 7). The filter applied is a 3rd order Butterworth high-pass filter with cutoff frequency 0.01Hz. Faint lines are extended-source and dark lines are point-source. The dominant contribution in the filtered signal is now arising from the conduit force, rather than chamber force.

7 Effects of instrument response

The synthetic seismograms presented in earlier sections feature a wide range of time scales, including contributions from the weight change and depressurization occurring over minutes to tens of minutes and even a static response. These may be challenging or impossible to observe, especially with short period instruments. Broadband seismometers can potentially go to much longer periods, if one corrects for instrument response. That said, the majority of volcano seismology studies of VLP events work with band-passed seismograms. Here we examine how the seismograms change if we remove low frequencies. To simulate the effect of instrument response on the observed signal, we apply a 3rd order Butterworth high-pass filter with a cutoff frequency 0.01 Hz to the velocity seismograms shown in Figure 7. The results are shown in Figure 16.

As expected, high-pass filtering emphasizes the contribution from the early stages of the eruption, where the seismogram is controlled by changes in shear traction and pressure in the top portion of the conduit. The conduit force largely dominates the filtered signal, with the conduit depressurization moment contribution becoming comparable at the tail-end of the signal on the radial component. There is no longer any information constraining the change in weight or even the chamber depressurization, as those occur over much greater time scales. This simple example demonstrates the bias, or at least limited view of the eruption process, that might be introduced in volcano seismology studies when working with band-limited data.

8 Discussion

Our workflow to generate synthetic seismograms from conduit flow and chamber models offers many new opportunities for studying explosive volcanic eruptions. While

the conduit flow model used in our example simulations is relatively simple, we believe it captures most of the fundamental eruptive processes that can be studied using seismic waves. Here we discuss the implications of our work and offer suggestions for future research directions.

8.1 Joint inversions of seismic, acoustic, and internal gravity waves using eruption modeling

Foremost, our workflow opens the possibility of complementing kinematic inversions of seismic data for independent force and moment histories with inversions that directly employ conduit flow models to self-consistently predict both force and moment histories. Similar efforts are being pursued using quasi-steady conduit flow models to connect with deformation data and other observations (K. Anderson & Segall, 2011, 2013; Segall, 2013; K. R. Anderson & Poland, 2016). More recently, seismic and geodetic data from the 2018 Kilauea caldera collapse events have been inverted using a dynamic source model of the caldera block dropping into an underlying reservoir, producing both a seismic force and moment tensor from which synthetic seismograms were constructed (Wang et al., 2021). In fact, their seismic source model can be viewed as a special case of ours. The down-dropping caldera block replaces the conduit magma in our model and is assumed to descend as a rigid body; changes in frictional tractions contribute to a vertical force (our F_{ch}), along with the force transmitted through the chamber magma to the solid Earth (the $-\Delta p_{ch}A$ contribution to F_{ch}). Because there is negligible mass loss, there is no change in weight or momentum transfer to the atmosphere. The seismic force is therefore most concisely written in the inertial-based representation as $F_s = -\dot{P}$, showing that it must start and end at zero. Pressurization of the chamber provides a moment tensor source, exactly as in our model. One can envision using a Bayesian inversion of the sort used in the aforementioned studies to invert VLP seismic data from explosive eruptions for parameters characterizing restraining tractions from a plug, volatile content and viscosity of the magma, parameters controlling fragmentation, chamber depth and size, etc.

There is also an opportunity for self-consistent joint inversions of multiple data sets. For example, infrasound and visual observations have been used to determine the rate at which the eruptive jets and plumes displace the surrounding atmosphere (Johnson & Miller, 2014; Kim et al., 2015; Fee, Izbekov, et al., 2017; A. Iezzi et al., 2019). This acoustic monopole source contribution can then be used to infer the eruptive mass rate by correcting for entrainment and expansion from heating, which requires assumptions. It seems possible to reduce uncertainty in the eruptive mass rate by seeking consistency with the seismically constrained eruptive mass rate from our new workflow.

In addition, advances in infrasound instrumentation deployments and inversions are placing constraints on dipole and higher order multipole acoustic sources (Jolly et al., 2017; A. Iezzi et al., 2019; A. M. Iezzi et al., 2022), which may be related to the momentum imparted to the atmosphere by the eruption. This momentum transfer is one contribution to the seismic force in the inertial-based representation (F_{vent}), and is therefore potentially constrainable from seismic waves using our modeling workflow.

In addition to infrasound (acoustic) waves, large volcanic eruptions also excite internal gravity waves in the atmosphere, which can be recorded on microbarometers, seismometers, and through changes in the total electron content of the ionosphere (Liu et al., 1982; Kanamori et al., 1994; Ripepe et al., 2010; Nakashima et al., 2016). These geophysical measurements can be inverted for mass and energy sources (Baines & Sacks, 2014; Ripepe et al., 2016). In addition, internal gravity waves will also be excited by a momentum source (F_{vent}), though this appears to have been neglected in previous work. All of these additional observational constraints could be integrated into a joint inver-

sion workflow in which the same source model is used to predict seismic, infrasound, and internal gravity waves, as well as visual observations of the jet and plume structure.

There is an opportunity to use simulations of the eruptive jet and atmospheric response (Ogden et al., 2008; Koyaguchi et al., 2018; Cerminara et al., 2016; Watson et al., 2021) as part of the forward modeling workflow to bypass assumptions and biases that may be introduced when using simple source models (e.g., point monopoles or dipoles; point mass, energy, and momentum sources) that are only indirectly linked to eruptive processes. To pursue this approach, we must develop coupled models of conduit flow and the response of a compressible atmosphere.

8.2 Band-limited seismograms provide a limited view of eruptive processes

Our work suggests that seismic data, from either short-period seismometers or broadband records filtered below 100 s, will be most useful in constraining shorter period, impulsive processes in eruptions. The filtered seismograms in Figure 16 are quite similar to those in some VLP studies, most notably of the 2004 Asama eruption for which inversions by Ohminato et al. (2006) identified a down-up-down vertical force of order 10^{10} N over approximately 10 s. Their conceptual explanation of the force history is similar to what is revealed in the first minute of our simulations. However, our work also suggests some caution when performing inversions of band-limited data and using those inversions to infer the eruptive source process. A key question is whether the inferred force and moment history from inversions of band-passed data will be a filtered version of the actual force and moment history. This will depend on how the inversion is set up. For an unconstrained, linear least squares inversion with given Green’s functions and source location, the inversion operator is linear with respect to model parameters F_i and M_{ij} and commutes with a filtering operator. In this case, the inverted force and moment histories will be filtered versions of the actual ones. However, most inversions are nonlinear with respect model parameters (e.g., source location or parameterized source time functions) and/or involve constraints that make the problem nonlinear. In this case, working with filtered data may lead to incorrect estimates of even the filtered force and moment histories.

Our models also predict seismic radiation at longer periods than can be resolved with short period seismometers, thereby emphasizing the importance of using broadband instruments and extending their bandwidth to longer periods than are commonly used by correcting for instrument response. This may permit quantification of the time history of the weight change, expressed in the seismic force, and depressurization of the conduit and chamber, expressed in the moment tensor. Constraints on depressurization could be compared to independent inversions using geodetic data, though we remark that the displacement amplitude from these sources may be too small to be measured with GNSS or InSAR, unless the chamber is sufficiently large.

Furthermore, the synthetic seismograms in this study were limited to distances no longer than a few tens of km from the source, and it will be important to extend our analysis to regional and teleseismic distances. Large explosive eruptions, like 1980 Mount St. Helens, 1991 Pinatubo, and the recent 2022 Hunga Tonga eruptions, generate seismic waves that can be recorded across Earth. We recommend that focus be placed at time scales of minutes to tens of minutes. Seismic waves at these ultra long periods are now widely used to characterize earthquake sources, for example through W-phase moment tensor inversions (Duputel et al., 2012). Similar inversions, but including a force, ought to be possible for large volcanic eruptions. It is unclear if trade-offs between the vertical force component and an axisymmetric moment tensor source, both radiating axisymmetric waves and subject to destructive interference of direct waves and free surface reflections, would render the inversion nonunique. In that case, the preferable alternative

is to replace inversions for independent force and moment with an actual eruption source model that self-consistently predicts force and moment, as articulated earlier.

8.3 Appropriateness of seismic force $F_s = -\dot{M}v$ thrust approximation

Brodsky et al. (1999), building on Kanamori and Given (1982), introduced the seismic force model $F_s \approx -\rho v^2 A$, evaluated at the vent. Defining the eruptive mass rate $\dot{M} = \rho v A$, this can be written as $F_s \approx -\dot{M}v$. This is often described as the thrust approximation, given its similarity to the thrust force provided by a jet engine. Prejean and Brodsky (2011) used this approximation to convert seismic inversions of F_s into estimates of \dot{M} for assumed values of the exit velocity v . The theory developed in Section 3 allows us to examine the validity of this approximation. We start with inertial-based representation of the seismic force given in equation (30): $F_s = -\dot{P} - F_{vent} - \Delta M g$, where $F_{vent} = \dot{M}v + \Delta p A$ at the vent. Brodsky et al. (1999) used a steady state eruption model to argue that $\Delta p A$ should be proportional to $\dot{M}v$, with the proportionality constant depending on Mach number at the vent. Uncertainty in the Mach number led to a factor of 4 uncertainty in their estimates of \dot{M} . Our models for small vulcanian eruptions show a similar proportionality between $\Delta p A$ and $\dot{M}v$ (Figure 6). However, we also find substantial contributions to F_s from the other terms in the representation, especially the weight change $-\Delta M g$. It is unclear how filtering (i.e., working with band-limited seismic data) would alter the seismic expression of the weight change contribution, and how this might map into errors or biases in eruptive mass rate histories inferred using the $F_s \approx -\dot{M}v$ approximation. Furthermore, we are generally most interested in the eruptive mass history, $\Delta M(t) = \int \dot{M} dt$, rather than the mass rate history, which requires integration of \dot{M} . One could approach this in a different manner by first performing inversions of ultra long period data, for which $F_s \approx -\Delta M g$, to determine $\Delta M(t)$. This could then be used as a constraint on inversions of shorter period data to more uniquely determine contributions from magma momentum changes, \dot{P} , and the two contributions, $\Delta p A$ and $\dot{M}v$, to F_{vent} .

8.4 High frequency seismic radiation

High frequency (> 1 Hz) radiation from volcanic eruptions has a stochastic character and is often described as eruptive tremor (McNutt & Nishimura, 2008; Fee, Haney, et al., 2017). Here we discuss how our modeling workflow might be used to better understand the origins of eruptive tremor and high frequency radiation.

First, fragmentation might contribute to eruptive tremor. Our simulations of eruptions with intermittent descent of the fragmentation front show large, high frequency seismic events. Each event is triggered by the abrupt fragmentation of a parcel of magma, loss of restraining tractions, and generation of upward tractions as the magma just below the fragmentation front accelerates. In our simulation, the timing of the fragmentation events, and details of the magma response and its reflection in the seismograms, is controlled by the grid spacing and the average speed of the descending fragmentation front. Thus, the time interval between successive fragmentation events increases as the fragmentation front decelerates. In reality, intermittent fragmentation will be determined by whatever heterogeneity temporarily impedes the fragmentation process, and we do not expect this to occur in a quasi-periodic manner as in our simulation. However, if the spatial scales characterizing the relevant heterogeneity are independent of depth, then we do expect a shift toward lower frequencies as the fragmentation front slows its descent.

High frequency seismic radiation during eruptions is also generated above fragmentation by turbulent pressure fluctuations and particle-wall interactions (McNutt & Nishimura, 2008; Fee, Haney, et al., 2017). Like the fragmentation process itself, these add a stochastic component to the seismic radiation. One could approach this problem by using con-

duit flow models that directly capture turbulence and particle-wall interactions (Dufek et al., 2012). Alternatively, one could combine simpler, quasi-1D conduit flow models of the sort used in our study together with some parameterization relating the unresolved turbulence and particle-wall interactions to the modeled mean flow. Seismic source models for these processes have been used in studies of streams, rivers, and debris flows (Burtin et al., 2008; Hsu et al., 2011; Tsai et al., 2012; Gimbert et al., 2014; Kean et al., 2015; Lai et al., 2018). Similar models, tailored for upper volcanic conduit flow, could be incorporated into conduit flow models.

It is presently unclear which processes provide the dominant control on eruptive tremor, but forward modeling efforts of the sort discussed above, combined with back-projection and related seismic array analyses to locate and track the source location of eruptive tremor, may be useful.

9 Conclusion

In this study, we derived two equivalent representations of the seismic force from volcanic eruptions and introduced a workflow for generating synthetic seismograms from models of unsteady magma flow in conduits and chambers. We applied the workflow to conduit flow models of small vulcanian eruptions. At periods of ~ 100 s and less, seismic radiation reflects unsteady processes in the conduit, such as loss of restraining tractions during rupture of plugs and upward drag from rapidly ascending magma. At longer periods, radiation is dominated by changes in the weight of magma remaining in the subsurface conduit-chamber system (producing an upward seismic force) and depressurization of the conduit and chamber (reflected in a moment tensor source). This new workflow offers many exciting possibilities for inverting seismic data using conduit flow models as part of the forward modeling process, thereby complementing or even circumventing inversions for independent force and moment histories.

References

- Aki, K., & Richards, P. G. (2002). *Quantitative Seismology*. University Science Books.
- Allstadt, K. (2013). Extracting source characteristics and dynamics of the August 2010 Mount Meager landslide from broadband seismograms. *Journal of Geophysical Research: Earth Surface*, 118(3), 1472–1490.
- Anderson, K., & Segall, P. (2011). Physics-based models of ground deformation and extrusion rate at effusively erupting volcanoes. *Journal of Geophysical Research: Solid Earth*, 116(B7).
- Anderson, K., & Segall, P. (2013). Bayesian inversion of data from effusive volcanic eruptions using physics-based models: Application to Mount St. Helens 2004–2008. *Journal of Geophysical Research: Solid Earth*, 118(5), 2017–2037.
- Anderson, K. R., & Poland, M. P. (2016). Bayesian estimation of magma supply, storage, and eruption rates using a multiphysical volcano model: Kīlauea Volcano, 2000–2012. *Earth and Planetary Science Letters*, 447, 161–171.
- Baines, P. G., & Sacks, S. (2014). Atmospheric internal waves generated by explosive volcanic eruptions. *Geological Society, London, Memoirs*, 39(1), 153–168.
- Brodsky, E. E., Kanamori, H., & Sturtevant, B. (1999). A seismically constrained mass discharge rate for the initiation of the May 18, 1980 Mount St. Helens eruption. *Journal of Geophysical Research: Solid Earth*, 104(B12), 29387–29400.
- Burridge, R., Kostek, S., & Kurkjian, A. L. (1993). Tube waves, seismic waves and effective sources. *Wave Motion*, 18(2), 163–210.
- Burtin, A., Bollinger, L., Vergne, J., Cattin, R., & Nábělek, J. (2008). Spectral analysis of seismic noise induced by rivers: A new tool to monitor spatiotemporal changes in stream hydrodynamics. *Journal of Geophysical Research: Solid Earth*, 113(B5).
- Carpenter, M. H., Gottlieb, D., & Abarbanel, S. (1994). Time-stable boundary conditions for finite-difference schemes solving hyperbolic systems: Methodology and application to high-order compact schemes. *Journal of Computational Physics*, 111, 220–236.
- Cerminara, M., Ongaro, T. E., & Neri, A. (2016). Large Eddy Simulation of gas-particle kinematic decoupling and turbulent entrainment in volcanic plumes. *Journal of Volcanology and Geothermal Research*, 326, 143–171.
- Chouet, B., Dawson, P., & Arciniega-Ceballos, A. (2005). Source mechanism of vulcanian degassing at Popocatepetl Volcano, Mexico, determined from waveform inversions of very long period signals. *Journal of Geophysical Research: Solid Earth*, 110(B7).
- Chouet, B. A., & Matoza, R. S. (2013). A multi-decadal view of seismic methods for detecting precursors of magma movement and eruption. *Journal of Volcanology and Geothermal Research*, 252, 108–175.
- Costa, A., Melnik, O., & Sparks, R. (2007). Controls of conduit geometry and wall-rock elasticity on lava dome eruptions. *Earth and Planetary Science Letters*, 260(1-2), 137–151.
- Dahlen, F. A. (1993). Single-force representation of shallow landslide sources. *Bulletin of the Seismological Society of America*, 83(1), 130–143.
- Dawson, P. B., Chouet, B. A., & Power, J. (2011). Determining the seismic source mechanism and location for an explosive eruption with limited observational data: Augustine Volcano, Alaska. *Geophysical Research Letters*, 38(3).
- Day, S. M., & McLaughlin, K. L. (1991). Seismic source representations for spall. *Bulletin of the Seismological Society of America*, 81(1), 191–201.
- De Angelis, S., Bass, V., Hards, V., & Ryan, G. (2007). Seismic characterization of pyroclastic flow activity at Soufrière Hills Volcano, Montserrat, 8 January 2007. *Natural Hazards and Earth System Sciences*, 7(4), 467–472.

- Del Rey Fernández, D. C., Hicken, J. E., & Zingg, D. W. (2014). Review of summation-by-parts operators with simultaneous approximation terms for the numerical solution of partial differential equations. *Computers & Fluids*, *95*, 171–196.
- Dufek, J., Manga, M., & Patel, A. (2012). Granular disruption during explosive volcanic eruptions. *Nature Geoscience*, *5*(8), 561–564.
- Duputel, Z., Rivera, L., Kanamori, H., & Hayes, G. (2012). W phase source inversion for moderate to large earthquakes (1990–2010). *Geophysical Journal International*, *189*(2), 1125–1147.
- Eissler, H. K., & Kanamori, H. (1987). A single-force model for the 1975 Kalapana, Hawaii, Earthquake. *Journal of Geophysical Research: Solid Earth*, *92*(B6), 4827–4836.
- Fee, D., Haney, M. M., Matoza, R. S., Van Eaton, A. R., Cervelli, P., Schneider, D. J., & Iezzi, A. M. (2017). Volcanic tremor and plume height hysteresis from Pavlof Volcano, Alaska. *Science*, *355*(6320), 45–48.
- Fee, D., Izbekov, P., Kim, K., Yokoo, A., Lopez, T., Prata, F., . . . Iguchi, M. (2017). Eruption mass estimation using infrasound waveform inversion and ash and gas measurements: Evaluation at Sakurajima Volcano, Japan. *Earth and Planetary Science Letters*, *480*, 42–52.
- Fontaine, F. R., Roult, G., Hejrani, B., Michon, L., Ferrazzini, V., Barruol, G., . . . others (2019). Very-and ultra-long-period seismic signals prior to and during caldera formation on La Réunion Island. *Scientific Reports*, *9*(1), 1–15.
- Fukao, Y., Sandanbata, O., Sugioka, H., Ito, A., Shiobara, H., Watada, S., & Satake, K. (2018). Mechanism of the 2015 volcanic tsunami earthquake near Torishima, Japan. *Science Advances*, *4*(4), eaao0219.
- Gimbert, F., Tsai, V. C., & Lamb, M. P. (2014). A physical model for seismic noise generation by turbulent flow in rivers. *Journal of Geophysical Research: Earth Surface*, *119*(10), 2209–2238.
- Haney, M. M., Chouet, B. A., Dawson, P. B., & Power, J. A. (2013). Source characterization for an explosion during the 2009 eruption of Redoubt Volcano from very-long-period seismic waves. *Journal of Volcanology and Geothermal Research*, *259*, 77–88.
- Hasegawa, H., & Kanamori, H. (1987). Source mechanism of the magnitude 7.2 Grand Banks Earthquake of November 1929: Double couple or submarine landslide? *Bulletin of the Seismological Society of America*, *77*(6), 1984–2004.
- Hsu, L., Finnegan, N. J., & Brodsky, E. E. (2011). A seismic signature of river bed-load transport during storm events. *Geophysical Research Letters*, *38*(13).
- Ichihara, M., Kusakabe, T., Kame, N., & Kumagai, H. (2016). On volume-source representations based on the representation theorem. *Earth, Planets and Space*, *68*(1), 1–10.
- Iezzi, A., Fee, D., Kim, K., Jolly, A., & Matoza, R. (2019). Three-dimensional acoustic multipole waveform inversion at Yasur Volcano, Vanuatu. *Journal of Geophysical Research: Solid Earth*, *124*(8), 8679–8703.
- Iezzi, A. M., Matoza, R. S., Fee, D., Kim, K., & Jolly, A. D. (2022). Synthetic evaluation of infrasonic multipole waveform inversion. *Journal of Geophysical Research: Solid Earth*, e2021JB023223.
- Johnson, J. B., & Miller, A. J. (2014). Application of the monopole source to quantify explosive flux during vulcanian explosions at Sakurajima Volcano (Japan). *Seismological Research Letters*, *85*(6), 1163–1176.
- Jolly, A. D., Matoza, R. S., Fee, D., Kennedy, B. M., Iezzi, A. M., Fitzgerald, R. H., . . . Johnson, R. (2017). Capturing the acoustic radiation pattern of strombolian eruptions using infrasound sensors aboard a tethered aerostat, Yasur Volcano, Vanuatu. *Geophysical Research Letters*, *44*(19), 9672–9680.
- Kanamori, H., & Given, J. W. (1982). Analysis of long-period seismic waves excited by the May 18, 1980, eruption of Mount St. Helens—A terrestrial monopole?

- 1049 *Journal of Geophysical Research: Solid Earth*, 87(B7), 5422–5432.
- 1050 Kanamori, H., Given, J. W., & Lay, T. (1984). Analysis of seismic body waves ex-
 1051 cited by the Mount St. Helens eruption of May 18, 1980. *Journal of Geophysi-
 1052 cal Research: Solid Earth*, 89(B3), 1856–1866.
- 1053 Kanamori, H., Mori, J., & Harkrider, D. G. (1994). Excitation of atmospheric os-
 1054 cillations by volcanic eruptions. *Journal of Geophysical Research: Solid Earth*,
 1055 99(B11), 21947–21961.
- 1056 Kawakatsu, H., & Yamamoto, M. (2015). Volcano Seismology. *Earthquake Seismol-
 1057 ogy*, 389–419.
- 1058 Kean, J. W., Coe, J. A., Coviello, V., Smith, J. B., McCoy, S. W., & Arattano, M.
 1059 (2015). Estimating rates of debris flow entrainment from ground vibrations.
 1060 *Geophysical Research Letters*, 42(15), 6365–6372.
- 1061 Kim, K., Fee, D., Yokoo, A., & Lees, J. M. (2015). Acoustic source inversion to
 1062 estimate volume flux from volcanic explosions. *Geophysical Research Letters*,
 1063 42(13), 5243–5249.
- 1064 Koyaguchi, T., Suzuki, Y. J., Takeda, K., & Inagawa, S. (2018). The condition of
 1065 eruption column collapse: 2. Three-dimensional numerical simulations of erup-
 1066 tion column dynamics. *Journal of Geophysical Research: Solid Earth*, 123(9),
 1067 7483–7508.
- 1068 Kreiss, H.-O., & Scherer, G. (1974). Finite element and finite difference methods
 1069 for hyperbolic partial differential equations. *Mathematical Aspects of Finite El-
 1070 ements in Partial Differential Equations.*, Academic Press, Inc., 195–212.
- 1071 Kumagai, H., Palacios, P., Maeda, T., Castillo, D. B., & Nakano, M. (2009). Seismic
 1072 tracking of lahars using tremor signals. *Journal of Volcanology and Geothermal
 1073 Research*, 183(1-2), 112–121.
- 1074 Lai, V. H., Tsai, V. C., Lamb, M. P., Ulizio, T. P., & Beer, A. R. (2018). The seis-
 1075 mic signature of debris flows: Flow mechanics and early warning at Montecito,
 1076 California. *Geophysical Research Letters*, 45(11), 5528–5535.
- 1077 Lai, V. H., Zhan, Z., Brissaud, Q., Sandanbata, O., & Miller, M. S. (2021). Inflation
 1078 and asymmetric collapse at Kilauea summit during the 2018 eruption from
 1079 seismic and infrasound analyses. *Journal of Geophysical Research: Solid Earth*,
 1080 126(10), e2021JB022139.
- 1081 Legrand, D., & Pertou, M. (2022). What are VLP signals at Stromboli Volcano?
 1082 *Journal of Volcanology and Geothermal Research*, 421, 107438.
- 1083 Liu, C., Klostermeyer, J., Yeh, K., Jones, T., Robinson, T., Holt, O., ... others
 1084 (1982). Global dynamic responses of the atmosphere to the eruption of Mount
 1085 St. Helens on May 18, 1980. *Journal of Geophysical Research: Space Physics*,
 1086 87(A8), 6281–6290.
- 1087 Maeda, Y., Takeo, M., & Kazahaya, R. (2019). Comparison of high-and low-
 1088 frequency signal sources for very-long-period seismic events at Asama Volcano,
 1089 Japan. *Geophysical Journal International*, 217(1), 389–404.
- 1090 Mastin, L. G. (2002). Insights into volcanic conduit flow from an open-source nu-
 1091 merical model. *Geochemistry, Geophysics, Geosystems*, 3(7), 1–18.
- 1092 Matoza, R. S., Chouet, B. A., Jolly, A. D., Dawson, P. B., Fitzgerald, R. H.,
 1093 Kennedy, B. M., ... others (2022). High-rate very-long-period seismicity
 1094 at Yasur Volcano, Vanuatu: Source mechanism and decoupling from surficial
 1095 explosions and infrasound. *Geophysical Journal International*.
- 1096 Mattsson, K. (2017). Diagonal-norm upwind SBP operators. *Journal of Computa-
 1097 tional Physics*, 335, 283–310.
- 1098 McNutt, S. R., & Nishimura, T. (2008). Volcanic tremor during eruptions: Tempo-
 1099 ral characteristics, scaling and constraints on conduit size and processes. *Jour-
 1100 nal of Volcanology and Geothermal Research*, 178(1), 10–18.
- 1101 McNutt, S. R., & Roman, D. C. (2015). Volcanic Seismicity. In *The Encyclopedia of
 1102 Volcanoes* (pp. 1011–1034). Elsevier.
- 1103 Melnik, O., & Sparks, R. (2002). Dynamics of magma ascent and lava extrusion

- at Soufrière Hills Volcano, Montserrat. In *The eruption of Soufrière Hills Volcano, Montserrat, from 1995 to 1999* (Vol. 21, pp. 153–171). Geological Society of London.
- Murray, T., Nettles, M., Selmes, N., Cathles, L., Burton, J. C., James, T. D., . . . others (2015). Reverse glacier motion during iceberg calving and the cause of glacial earthquakes. *Science*, *349*(6245), 305–308.
- Nakashima, Y., Heki, K., Takeo, A., Cahyadi, M. N., Aditiya, A., & Yoshizawa, K. (2016). Atmospheric resonant oscillations by the 2014 eruption of the Kelud Volcano, Indonesia, observed with the ionospheric total electron contents and seismic signals. *Earth and Planetary Science Letters*, *434*, 112–116.
- Nettles, M., & Ekström, G. (2010). Glacial earthquakes in Greenland and Antarctica. *Annual Review of Earth and Planetary Sciences*, *38*, 467–491.
- Ogden, D. E., Glatzmaier, G. A., & Wohletz, K. H. (2008). Effects of vent overpressure on buoyant eruption columns: Implications for plume stability. *Earth and Planetary Science Letters*, *268*(3–4), 283–292.
- Ohminato, T., Takeo, M., Kumagai, H., Yamashina, T., Oikawa, J., Koyama, E., . . . Urabe, T. (2006). Vulcanian eruptions with dominant single force components observed during the Asama 2004 volcanic activity in Japan. *Earth, Planets and Space*, *58*(5), 583–593.
- Prejean, S. G., & Brodsky, E. E. (2011). Volcanic plume height measured by seismic waves based on a mechanical model. *Journal of Geophysical Research: Solid Earth*, *116*(B1).
- Ripepe, M., Barfucci, G., De Angelis, S., Delle Donne, D., Lacanna, G., & Marchetti, E. (2016). Modeling volcanic eruption parameters by near-source internal gravity waves. *Scientific Reports*, *6*(1), 1–8.
- Ripepe, M., De Angelis, S., Lacanna, G., & Voight, B. (2010). Observation of infrasonic and gravity waves at Soufrière Hills Volcano, Montserrat. *Geophysical Research Letters*, *37*(19).
- Ripepe, M., Delle Donne, D., Legrand, D., Valade, S., & Lacanna, G. (2021). Magma pressure discharge induces very long period seismicity. *Scientific Reports*, *11*(1), 1–12.
- Roman, D. C., & Cashman, K. V. (2006). The origin of volcano-tectonic earthquake swarms. *Geology*, *34*(6), 457–460.
- Sandanbata, O., Kanamori, H., Rivera, L., Zhan, Z., Watada, S., & Satake, K. (2021). Moment tensors of ring-faulting at active volcanoes: Insights into vertical-CLVD earthquakes at the Sierra Negra Caldera, Galápagos Islands. *Journal of Geophysical Research: Solid Earth*, *126*(6), e2021JB021693.
- Segall, P. (2010). *Earthquake and Volcano Deformation*. Princeton University Press.
- Segall, P. (2013). Volcano deformation and eruption forecasting. *Geological Society, London, Special Publications*, *380*(1), 85–106.
- Takei, Y., & Kumazawa, M. (1994). Why have the single force and torque been excluded from seismic source models? *Geophysical Journal International*, *118*(1), 20–30.
- Takei, Y., & Kumazawa, M. (1995). Phenomenological representation and kinematics of general seismic sources including the seismic vector modes. *Geophysical Journal International*, *121*(3), 641–662.
- Takeo, M., Yamasato, H., Furaya, I., & Seino, M. (1990). Analysis of long-period seismic waves excited by the November 1987 eruption of Izu-Oshima Volcano. *Journal of Geophysical Research: Solid Earth*, *95*(B12), 19377–19393.
- Tsai, V. C., Minchew, B., Lamb, M. P., & Ampuero, J.-P. (2012). A physical model for seismic noise generation from sediment transport in rivers. *Geophysical Research Letters*, *39*(2).
- Tsai, V. C., Rice, J. R., & Fahnstock, M. (2008). Possible mechanisms for glacial earthquakes. *Journal of Geophysical Research: Earth Surface*, *113*(F3).
- Uhira, K., & Takeo, M. (1994). The source of explosive eruptions of Sakurajima

- Volcano, Japan. *Journal of Geophysical Research: Solid Earth*, 99(B9), 17775–17789.
- Wang, T., Coppess, K., Segall, P., Dunham, E. M., & Ellsworth, W. L. (2021). Physics-based model reconciles caldera collapse induced static and dynamic ground motion: Application to Ilauea 2018. *Earth and Space Science Open Archive*, 15.
- Watson, L. M., Dunham, E. M., Mohaddes, D., Labahn, J., Jaravel, T., & Ihme, M. (2021). Infrasound radiation from impulsive volcanic eruptions: Nonlinear aeroacoustic 2D simulations. *Journal of Geophysical Research: Solid Earth*, 126(9), e2021JB021940.
- Watson, L. M., Werpers, J., & Dunham, E. M. (2019). What controls the initial peak of an air-gun source signature? *Geophysics*, 84(2), P27–P45.
- Wilson, L., & Head III, J. W. (1981). Ascent and eruption of basaltic magma on the Earth and Moon. *Journal of Geophysical Research: Solid Earth*, 86(B4), 2971–3001.
- Wilson, L., Sparks, R. S. J., & Walker, G. P. (1980). Explosive volcanic eruptions—IV. The control of magma properties and conduit geometry on eruption column behaviour. *Geophysical Journal International*, 63(1), 117–148.
- Woods, A. W. (1995). The dynamics of explosive volcanic eruptions. *Reviews of Geophysics*, 33(4), 495–530.
- Yamasato, H. (1997). Quantitative analysis of pyroclastic flows using infrasonic and seismic data at Unzen Volcano, Japan. *Journal of Physics of the Earth*, 45(6), 397–416.
- Zhu, L., & Rivera, L. A. (2002). A note on the dynamic and static displacements from a point source in multilayered media. *Geophysical Journal International*, 148(3), 619–627.
- Zobin, V. M., Plascencia, I., Reyes, G., & Navarro, C. (2009). The characteristics of seismic signals produced by lahars and pyroclastic flows: Volcán de Colima, México. *Journal of Volcanology and Geothermal Research*, 179(1-2), 157–167.

Acknowledgments

This work was supported by National Science Foundation grants EAR-1930979 (E.M.D.) and DGE-1656518 (K.R.C.). We thank Paul Segall and Taiyi Wang for useful discussions of the single force in caldera collapse events and momentum transfer through magma chambers.

Data Availability Statement

The simulation data and analysis code for this work are hosted at the Open Science Framework (doi: 10.17605/OSF.IO/R6HJC) and <https://bitbucket.org/kcoppess/synthetic-seismograms/src/conduit-flow/>.

Appendix A Derivation of volcanic source representation

Conduit flow models capture the evolution of pressure and shear traction along the conduit throughout an eruption. In this appendix, we derive expressions that convert pressure and shear traction changes to equivalent moment tensor and force sources for use in our seismic wave calculation. Our derivation closely follows Burridge et al. (1993), who studied seismic wave radiation from pressure changes in borehole filled with inviscid fluid. Our derivation extends their work by accounting for shear tractions that manifest in a seismic force. For simplicity, we restrict attention to a straight, cylindrical conduit of radius R and cross-sectional area $A = \pi R^2$ oriented along the z axis contained within an elastic medium.

The conduit radius is assumed small in comparison to the wavelengths of deformation and waves outside the conduit, their ratio denoted as ϵ . It is well known that when $\epsilon \ll 1$, fluid motions within the conduit are well described with quasi-1D models in which changes in pressure Δp and shear traction $\Delta \tau$ depend only on z and t . The elastic compliance of the walls appears in this solution through a local (at each z) 2D elastostatic response. This additional compliance is generally negligible in comparison to magma compressibility for cylindrical conduits but may be important for dike-like conduits (e.g., Costa et al., 2007). This quasi-1D approximation forms the basis of most volcanic conduit flow models in the literature (e.g., Wilson & Head III, 1981; Melnik & Sparks, 2002; Woods, 1995; Mastin, 2002), including the one in our study, and we assume in the derivation to follow that Δp and $\Delta \tau$ are known from solving such a model.

Our objective is to determine the equivalent body force distribution f_i that appears in the elastic wave equation, describing the response of an idealized model Earth in which the conduit is replaced with elastic material (Takei & Kumazawa, 1994):

$$\rho \frac{\partial^2 u_i}{\partial t^2} - \frac{\partial}{\partial x_j} \left(C_{ijkl} \frac{\partial u_k}{\partial x_l} \right) = f_i, \quad (\text{A1})$$

where ρ is the density of the elastic solid and C_{ijkl} is the stiffness tensor. When $\epsilon \ll 1$, we anticipate that f_i will be a singular distribution involving delta functions and their derivatives that localize the source to the z axis, namely

$$f_i(\mathbf{x}, t) = \frac{\partial F_i(z, t)}{\partial z} \delta(x) \delta(y) - \frac{\partial M_{ij}(z, t)}{\partial z} \frac{\partial}{\partial x_j} \delta(x) \delta(y), \quad (\text{A2})$$

where $\partial F_i / \partial z$ and $\partial M_{ij} / \partial z$ are the force and seismic moment tensor per unit distance along the conduit. Thus u_i must be regarded as a weak solution that is not differentiable at the z axis. An appropriate starting point is the weak form of (A1) given in equation (4.2) of Burridge et al. (1993):

$$I = \iint_V \phi_i f_i dV dt \quad (\text{A3})$$

$$= \iint_V \left[\rho \frac{\partial^2 \phi_i}{\partial t^2} - \frac{\partial}{\partial x_l} \left(C_{ijkl} \frac{\partial \phi_i}{\partial x_j} \right) \right] u_k d^3x dt, \quad (\text{A4})$$

where ϕ_i is a infinitely differentiable test function, the volume V includes the conduit region in which u_i is defined to be zero, and the time integral is over all time. Inserting the anticipated body force distribution (A2) into (A3) and integrating by parts gives

$$I = \iint \left(\phi_i \frac{\partial F_i}{\partial z} + \frac{\partial \phi_i}{\partial x_j} \frac{\partial M_{ij}}{\partial z} \right) dz dt. \quad (\text{A5})$$

The goal of the derivation to follow is to identify $\partial F_i / \partial z$ and $\partial M_{ij} / \partial z$ by manipulating (A4), together with interface conditions on the conduit walls and an asymptotic expansion for narrow conduits, into the form of (A5).

Burridge et al. (1993) use the divergence theorem, definition of u_i as zero within the conduit, and vanishing of f_i outside the conduit to rewrite (A4) as

$$I = \iint_{\Sigma} \left(\frac{\partial \phi_i}{\partial x_j} C_{ijkl} u_k n_l - \phi_i C_{ijkl} \frac{\partial u_k}{\partial x_l} n_j \right) d^2x dt, \quad (\text{A6})$$

where Σ is the surface of the conduit and the unit normal n_i to Σ points outward from the conduit into the solid. Thus far no approximations have been made. We Taylor expand C_{ijkl} and ϕ_i in the two horizontal dimensions about z axis, keeping only leading order terms in ϵ , and utilize the interface traction condition, expressed to leading order as

$$C_{ijkl} \frac{\partial u_k}{\partial x_l} n_j = -\Delta p n_i - \Delta \tau \delta_{iz}. \quad (\text{A7})$$

Defining $\partial\Sigma$ as the perimeter of the conduit at fixed z and s as the arclength along $\partial\Sigma$, we obtain

$$I = \iiint_{\partial\Sigma} \left\{ \frac{\partial\phi_i}{\partial x_j} [C_{ijkl}u_k n_l + x_j(\Delta p n_i + \Delta\tau\delta_{iz})] + \phi_i(\Delta p n_i + \Delta\tau\delta_{iz}) \right\} ds dz dt, \quad (\text{A8})$$

where C_{ijkl} , ϕ_i , $\partial\phi_i/\partial x_j$ are now evaluated on the z axis and are independent of s .

Burridge et al. (1993) also show that boundary displacements u_i along the walls of the conduit, as appear in (A8), and just outside it are described, to leading order in ϵ , by a locally 2D elastostatic response at fixed z , namely

$$\frac{\partial\sigma_{i\alpha}}{\partial x_\alpha} = 0, \quad \sigma_{ij} = C_{ijk\alpha} \frac{\partial u_k}{\partial x_\alpha}, \quad (\text{A9})$$

where $\alpha = x, y$, subject to the traction condition (A7). Next we specialize to an isotropic solid, such that

$$C_{ijkl}u_k n_l = \lambda\delta_{ij}u_k n_k + \mu(u_i n_j + u_j n_i), \quad (\text{A10})$$

and the 2D elastostatic problem decomposes into the familiar plane strain and antiplane shear problems with traction boundary conditions (A7). The plane strain problem produces radial displacement

$$u_r = \frac{R^2 \Delta p}{2\mu r} \quad (\text{A11})$$

and the antiplane shear problem produces vertical displacement

$$u_z = \frac{\Delta\tau R}{\mu} \ln(R_\infty/r), \quad (\text{A12})$$

where r is the radial distance from $z = 0$ and the conduit wall is at $r = R$. For the plane strain problem, $u_r \rightarrow 0$ as $r \rightarrow \infty$. However, for the antiplane shear problem, we set $u_z = 0$ at $r = R_\infty$, where R_∞ is assumed to be much larger than R . The choice of R_∞ is irrelevant, as it drops out of the problem in the next step.

We utilize this asymptotic elastostatic solution to evaluate the following integrals that appear in (A8):

$$\int_{\partial\Sigma} u_k n_k ds = \frac{\Delta p A}{\mu}, \quad \int_{\partial\Sigma} (u_i n_j + u_j n_i) ds = \frac{\Delta p A}{\mu} (\delta_{ij} - \delta_{iz}\delta_{jz}), \quad (\text{A13})$$

$$\int_{\partial\Sigma} x_j n_i ds = A(\delta_{ij} - \delta_{iz}\delta_{jz}), \quad \int_{\partial\Sigma} x_j \delta_{iz} ds = 0. \quad (\text{A14})$$

It follows that

$$\int_{\partial\Sigma} [C_{ijkl}u_k n_l + x_j(\Delta p n_i + \Delta\tau\delta_{iz})] ds = \frac{\Delta p A}{\mu} [(\lambda + 2\mu)\delta_{ij} - 2\mu\delta_{iz}\delta_{jz}] \quad (\text{A15})$$

and hence (A8) becomes

$$I = \iint \left\{ \frac{\partial\phi_i}{\partial x_j} \frac{\Delta p A}{\mu} [(\lambda + 2\mu)\delta_{ij} - 2\mu\delta_{iz}\delta_{jz}] + \phi_i 2\pi R \Delta\tau \delta_{iz} \right\} dz dt. \quad (\text{A16})$$

Comparing to (A2), we identify

$$\frac{\partial F_i}{\partial z} = 2\pi R \Delta\tau \delta_{iz}, \quad \frac{\partial M_{ij}}{\partial z} = \frac{\Delta p A}{\mu} [(\lambda + 2\mu)\delta_{ij} - 2\mu\delta_{iz}\delta_{jz}]. \quad (\text{A17})$$